



저작자표시-비영리-변경금지 2.0 대한민국

이용자는 아래의 조건을 따르는 경우에 한하여 자유롭게

- 이 저작물을 복제, 배포, 전송, 전시, 공연 및 방송할 수 있습니다.

다음과 같은 조건을 따라야 합니다:



저작자표시. 귀하는 원저작자를 표시하여야 합니다.



비영리. 귀하는 이 저작물을 영리 목적으로 이용할 수 없습니다.



변경금지. 귀하는 이 저작물을 개작, 변형 또는 가공할 수 없습니다.

- 귀하는, 이 저작물의 재이용이나 배포의 경우, 이 저작물에 적용된 이용허락조건을 명확하게 나타내어야 합니다.
- 저작권자로부터 별도의 허가를 받으면 이러한 조건들은 적용되지 않습니다.

저작권법에 따른 이용자의 권리는 위의 내용에 의하여 영향을 받지 않습니다.

이것은 [이용허락규약\(Legal Code\)](#)을 이해하기 쉽게 요약한 것입니다.

[Disclaimer](#)

이학박사 학위논문

**Consolidation of magneto-optic
measurement methods for spin-torque
quantification**

광학적 스핀-궤도 돌림힘
측정 방법의 통합

2019년 2월

서울대학교 대학원

물리천문학부

김 주 성

Consolidation of magneto-optic measurement methods for spin-torque quantification

Joo-Sung Kim

Supervised by
Professor Sug-Bong Choe

A Dissertation in Physics

Submitted to the Faculties of
Seoul National University
in Partial Fulfillment of the Requirements for the Degree of
Doctor of Philosophy

February 2019

*Department of Physics and Astronomy
The Graduate College of Natural Sciences
Seoul National University*

Abstract

Spin-orbit torque (SOT) is an interaction between the magnetization and spin currents that is generated from the material with spin-orbit interaction. A number of researches have been investigated since SOT enables current control of the magnetization, which is crucial component for the scaling of the spintronic memory devices.

Quantification of the SOT could be realized in various configurations such as current-induced magnetization switching, current-induced domain wall motion (CIDWM), spin-torque ferromagnetic resonance (ST-FMR), and current-induced oscillation in $\omega - 2\omega$ measurement method. Various values of the SOT have been obtained from samples with various materials and from different measurement methods.

To obtain the exact value of SOT, we compared the results from different SOT measurement methods for cross-check. Two methods based on DWM and $\omega - 2\omega$ measurement method have been adopted to measure SOT in samples with 7 different materials. By comparing the results, we confirmed experimentally the conversion factor between the SOT values that had been expected theoretically.

We also developed an artifact-free optical SOT measurement method to resolve the problems in electrical SOT measurement method. Planar Hall effect (PHE) and

anomalous Nernst effect (ANE) are two major artifacts that hinders exact analysis of SOT. By controlling the polarization state of light, we separated PHE-like signal from the polar magneto-optic Kerr effect (pMOKE) signal in measured intensity. This method excludes artifacts from the measured intensity whereas artifacts have been compensated after the measurement in the previous methods.

We expect that the cross-check between the SOT results from different methods and development of the artifact-free optical SOT measurement method would expand the range of the SOT study and could expand the knowledge on the underlying mechanism of SOT.

Keywords : spin-orbit torque (SOT), polar magneto-optic Kerr effect (pMOKE), planar Hall effect (PHE), anomalous Nernst effect (ANE)

Student number : 2013-20363

Contents

Abstract.....	iii
List of Figures	viii
List of Tables	x
1. Introduction.....	11
1.1 Magnetic Domain and Domain-Wall	12
1.2 Magneto-Optics and Magneto-Transports	14
1.3 Spin-Torques	17
2. Improvements and development of the MOKE setups to measure SOT induced phenomena in domain wall motions and harmonic measurements	20
2.1 Scanning MOKE Setup.....	21
2.1.1 Setup Specification.....	21
2.1.2 Types of Measurements Available for Scanning MOKE Microscope System	24
2.1.3 DW Writing Methods	26
2.2 Harmonic Measurement Setup.....	31
2.2.1 Setup Specification.....	31
2.2.2 Improvements of Harmonic Measurement Setup	33

3. Comparison between spin-orbit torques measured by domain-wall motions and harmonic measurements	45
3.1 Introduction	46
3.2 Experimental Details.....	47
3.3 Measurement of SOT in DWM.....	48
3.4 Measurement of SOT in HM	53
3.5 Comparison of SOT in DWM and HM	57
3.6 Conclusion.....	60
4. Development of artifact-free optical spin-orbit torque magnetometry	61
4.1 Introduction	62
4.2 Experimental Details.....	65
4.3 SOT Results with PEM on/off	66
4.4 Discussion for Elimination of Optic PHE and Optic ANE.....	77
4.5 Conclusion.....	81
5. Characterization of the magnetic samples.....	82
5.1 Introduction of Curie Temperature T_c Measurement System	83
5.2 Improvement on Perpendicular Anisotropy Field H_K^{eff} Measurement Method.....	87

5.3 TEM Image Measurement	89
Appendix	90
A.1 Jones Calculus for MOKE Signal	
References	94
국문 초록 (Abstract in Korean).....	97
Publications	99
Conferences	100

List of Figures

Figure 1.1.1 The image of patterned ultrathin magnetic wires with PMA.	12
Figure 1.2.1 An illustration of MOKE and AHE.	15
Figure 1.3.1 An illustration of the STT mechanism.....	18
Figure 1.3.2 An illustration of the SHE mechanism.	19
Figure 2.1.1 A schematic diagram of the scanning MOKE microscope and an image of the measurement system.....	21
Figure 2.1.2.1 A hysteresis loop of the sample with PMA.	25
Figure 2.1.2.2 Magnitude of SOT-induced loopshift.	26
Figure 2.1.3.1 An image of magnetic wire and electrodes.....	28
Figure 2.2.1.1 An image and a schematic diagram of the harmonic measurement setup.	32
Figure 2.2.2.1 Step-sine shape of the applied current.....	37
Figure 2.2.2.2 3D calibration data for 2-axis magnetic fields H_x and H_z	38
Figure 2.2.2.3 FFT noise profile before and after the installation of UPS system.	40
Figure 2.2.2.4 FFT noise profile before and after installation of the Faraday isolator.	41
Figure 2.2.2.5 FFT noise profiles of a HeNe laser and a diode laser.	42
Figure 2.2.2.6 Polar plot of the intensity with respect to the analyzer angle.....	43
Figure 2.2.2.7 Polar plot of the intensity with various HWP rotation angles.	44
Figure 3.3.1 Schematic drawing of measurement setup.	48
Figure 3.3.2 Plot of the MOKE signal with respect to H_z under constant current bias.	49
Figure 3.3.3 Plot of ν with respect to H_z under current bias.	50
Figure 3.3.4 Plot of $\varepsilon_{\text{DW}}^{(1)}$ (black) and $\varepsilon_{\text{DW}}^{(2)}$ (red) with respect to H_x	51

Figure 3.3.5 Plot of $\varepsilon_{\text{DW}}^{\text{sat}}$ for Pt/Co/X stacks.....	52
Figure 3.4.1 Plot of Δm_z with respect to t for several different H_x 's.....	54
Figure 3.4.2 Plot of Δm_z^{max} with respect to H_x	55
Figure 3.4.3 Plot of ε_L for Pt/Co/X stacks.....	56
Figure 3.5.1 Plot of $\varepsilon_{\text{DW}}^{\text{sat}}$ with respect to ε_L for Pt/Co/X stacks.....	57
Figure 4.3.1. A schematic diagram of the optical SOT measurement setup.	67
Figure 4.3.2 The SOT-induced signal $\Delta I_{\text{BD, IMA}}^{\text{off}}$ from various ϕ_{pol}	71
Figure 4.3.3 Linear proportionality of $\Delta A_{2f, \text{IMA}}$ with respect to J	74
Figure 4.3.4 Comparison of $\Delta A_{2f, \text{IMA}}$ and $\Delta I_{\text{BD, IMA}}^{\text{off}}$ versus ϕ_{pol}	75
Figure 5.1.1 An electric measurement system for characterization of T_c	84
Figure 5.1.2 The hysteresis loops of sample with temperature from 295 K to 347 K	85
Figure 5.1.3 The plot of m_r versus temperature with $t_{\text{Co}}= 0.3, 0.35, 0.4, 0.45$ nm.	86
Figure 5.2.1 m_z with respect to in-plane magnetic field H_y	88
Figure 5.3.1 Cross-sectional STEM image with EDS color map of the Pt/Co/Pt sample.	89

List of Tables

Table A.1.1 Jones matrices of optical components.	90
--	----

Chapter 1

Introduction

As energy scale of the interactions in researches decreases, systems regarding spins of the electrons have been investigated widely. Although the history of magnetism dates back to B.C. with primitive understanding, recent studies on spin-torques are intensely investigated due to the possibility of current control of the magnetization in nano-scale magnetic memory devices[1-6].

This thesis mainly covers the study about spin-orbit torque (SOT) phenomena and measurement methods in samples with ferromagnetism. In chapter 1, basic concepts for magnetism have been introduced. Magnetic domains and domain-walls are studied to reveal the underlying physics of magnetic interactions and spin-torques via measurements using magneto-optics and magneto-transport. In chapter 2, experimental setups to measure domain-wall motions and harmonic measurements have been presented as well as efforts to improve signal-to-noise ratio. In chapter 3, methods for spin-orbit torque (SOT) quantification have been compared to give conversion factor between results. In chapter 4, an optical SOT measurement method have been proposed to eliminate optic planar Hall effect that hinders analysis for electrical SOT measurements. In chapter 5, additional measurements for sample characterization have been introduced.

1.1 Magnetic Domain and Domain-Wall

For ferromagnetic samples, exchange interaction between local magnetizations favors the parallel alignment of the adjacent magnetizations. Magnetic domain and domain-wall (DW) are two major subjects of the studies throughout the thesis. A magnetic domain is formed in a region which has same direction of magnetization formed by the exchange interaction. Figure 1.1.1 shows the image of patterned ultrathin magnetic wires with perpendicular magnetic anisotropy (PMA) with up and down domains.



Figure 1.1.1 The image of patterned ultrathin magnetic wires with PMA. Dark (bright) region corresponds to up (down) domain.

A magnetic DW is a magnetic structure at the boundary of two domains of different polarity. A DW has Bloch type and Néel type chiral magnetic structures [7-9] that could be converted by applying external magnetic field or introducing

Dzyaloshinskii-Moriya interaction (DMI) [7-8, 12-15]. In 1D model that describes the behavior of a DW, DW is considered as quasi-particle[10-11]. Magnetic field and spin currents can exert torque to the magnetizations in a DW or domain, generating DW motion or tilting of the magnetization [1-2, 4, 7, 12-17, 18-27]. Measurement of DW motion or tilting of magnetization could be realized by electrical or optical detection principles as explained in Chapter 1.2.

1.2 Magneto-Optics and Magneto-Transports

Detection of magnetization is demonstrated by optical and electrical measurement methods. Magneto-optic and magneto-transport provide various methods to investigate magnetization dynamics to reveal underlying physics. Magneto-optic Kerr effect (MOKE) [28] is a magneto-optic interaction that induces change of the polarization state of the light upon reflection from the magnetized surface. The MOKE that occurs in the polar geometry with interaction between light of normal incidence and out-of-plane magnetization m_z is called polar MOKE (pMOKE) as shown in Figure 1.2.1.

When light propagates through a medium with magnetism, its normal modes are defined by left and right circular polarization (LCP, RCP)[29]. Complex indices of refraction have different values for two normal modes of LCP and RCP. Therefore reflected light from magnetized surface experiences polarization change with Kerr rotation θ_K and Kerr ellipticity ϵ_K from MOKE [30] whereas transmitted light from magnetized medium experiences rotation of the polarization known as the Faraday effect.

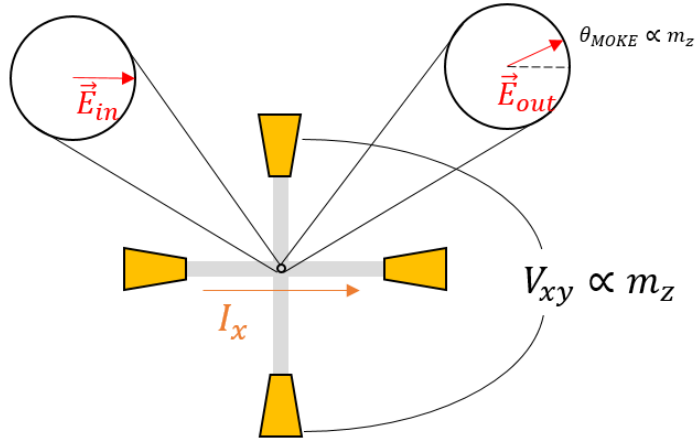


Figure 1.2.1 An illustration of the two magnetization-induced off-diagonal responses of MOKE and AHE.

Meanwhile, a magneto-transport effect known as anomalous Hall effect (AHE) has similar geometry with pMOKE [31]. As seen in Figure 1.2.1, if current flows in \hat{x} direction and transverse voltage V_{xy} is measured, signal proportional to the out-of-plane magnetization m_z is obtained.

Both effects of pMOKE and AHE can be interpreted as off-diagonal response induced by magnetization. The AHE induces transverse voltage that is perpendicular to the applied voltage whereas pMOKE induces transverse electric field of the reflected light that is perpendicular to the electric field of the incident light.

This analogy between magneto-optics and magneto-transport could be extended to the different form of response. Planar Hall effect (PHE) is another type of magneto-transport that generates transverse voltage V_{xy} that is proportional to the $m_x \cdot m_y$. PHE arises when anisotropic magnetoresistance (AMR) that induces change of the longitudinal resistance R_{xx} is present in a sample [32]. For samples such as W/CoFeB/MgO, the signal of PHE is even greater than AHE signal [33]. Therefore, analysis using AHE signal becomes complicated in a sample with sizable PHE. Similar effect to PHE has been reported in magneto-optics and method for eliminating optic PHE as well as difficulties accompanied would be discussed in Chapter 4.

1.3 Spin-Torques

Spin-torques are generic term for torque exerted on magnetization by spin current. Spin-torques have been intensely investigated due to the possibility of the current control of the magnetization for spintronic memory devices [1-6]. Depending on the mechanism for spin current generation, spin-torques can be divided into two main sub-categories of spin-transfer torque (STT) and spin-orbit torque (SOT).

STT occurs when a current flows through nonhomogeneous magnetization [34-36]. As illustrated in Figure 1.3.1, conduction electron with random spin direction interacts with the local magnetization in the first ferromagnetic layer (FM1) and spin-polarized current flows into the second ferromagnetic layer (FM2). Then the second interaction occurs to align the spin direction of the conduction electron as well as exert torque on a magnetization in FM2. Likewise, current that flows through a DW experiences successive alignment of spin to the chiral structure of the local magnetization and generates STT on a DW to cause current-induced domain-wall motion.

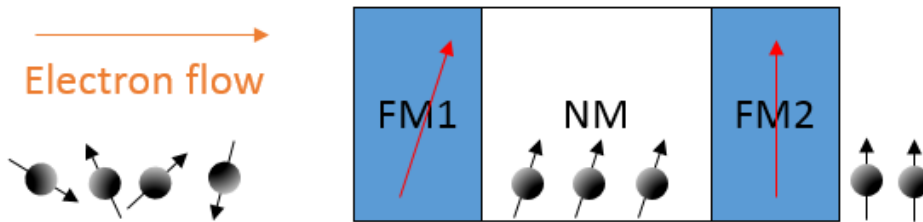


Figure 1.3.1 An illustration of the STT mechanism for current flows through two magnetic layers.

SOT is an interaction between the magnetization and spin current generated by spin-orbit interaction. The spin-orbit interaction mechanisms that generate spin current for SOT are divided into two pictures; spin-Hall effect (SHE) and Rashba effect pictures[7, 16, 18-20, 22, 37-43]. Figure 1.3.2 illustrates SHE picture for spin current generation. The current flows in the heavy metal (HM) layer and electrons experience spin-dependent scattering due to spin-orbit interaction. Therefore path of the electrons with different spin direction is separated. The accumulated spins by SHE at the boundaries of the HM diffuse and exert torque on the ferromagnetic layer (FM). For the case of the Rashba effect pictures, relativistic effect of Rashba field at the interface where the structural inversion symmetry is broken.

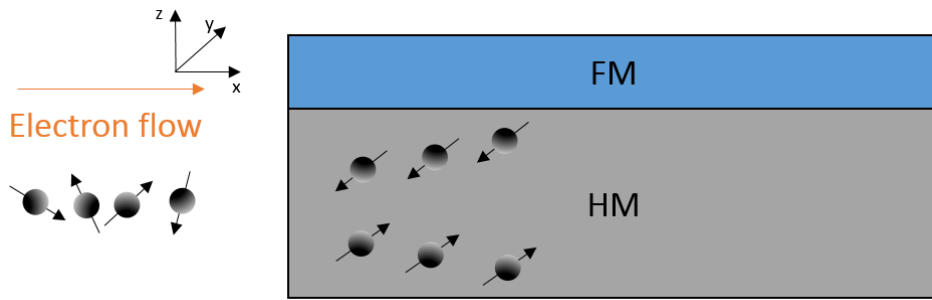


Figure 1.3.2 An illustration of the SHE mechanism of spin current generation for SOT.

Chapter 2

Improvements and development of the MOKE setups to measure SOT in domain-wall motions and harmonic measurements

The measurement methods of spin-torque-induced phenomena have been realized by utilizing two major principles for magnetization detection. Electrical methods from AHE signal and optical methods from MOKE signal have been developed to measure various phenomena such as current-induced domain-wall motion (CIDWM), loopshift, and SOT switching [1-2, 4, 7, 12-17, 41-45]. In this chapter, two types of MOKE setups have been presented as well as brief introductions of domain-wall motion (DWM) measurements and harmonic measurements (HM).

2.1 Scanning MOKE Setup

For the experiments regarding domain-wall motion measurement, a setup with scanning MOKE microscope has been used. This setup measures polar MOKE signal to detect out-of plane component of the magnetization in the sample. A schematic diagram of the scanning MOKE microscope system and actual image of the measurement system are presented in Figure 2.1.1.

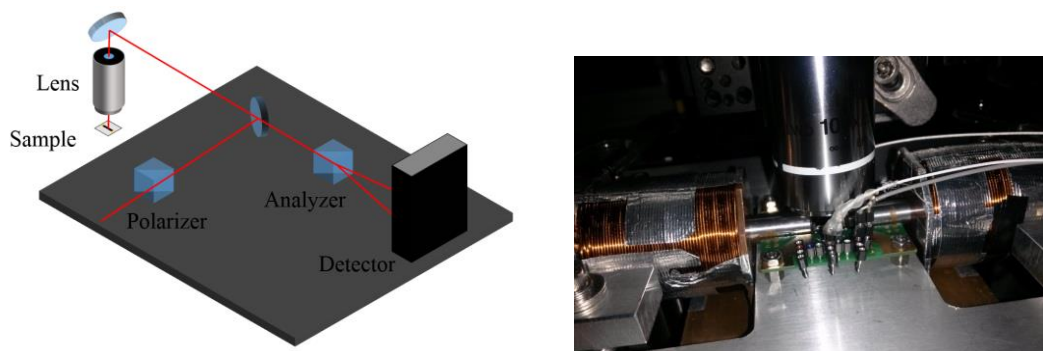


Figure 2.1.1 An image and a schematic diagram of the harmonic measurement setup with electromagnet and optical system for MOKE measurement.

2.1.1 Setup specification

A fiber-coupled laser with center wavelength of 780 nm (Thorlabs, S1FC780) has been used to provide a beam for probing. The optical power of the incident probing laser on the sample was kept less than $200\mu\text{W}$ to minimize heat-induced degrading of the sample or other thermal effects in DWM. A laser beam from the light source goes through the polarizer (Thorlabs, GL-10B) to determine the direction of the polarization of the light. The beam path leads to the normal incidence for the sample by reflection from the beam splitter (Thorlabs, BSW11) and focusing from the objective lens (Nikon, CFI L Plan EPI SLWD 100X, WD 6.5). Unlike the 2D microscopes, only the spherical aberration has been considered for the selection of the objective lens since the chromatic aberration does not happen in a system with monochromatic light. The spatial resolution defined by the Abbe (or Rayleigh) criterion ($r = 0.5 (0.61) \times \lambda/\text{NA}$) is given by $\sim 559 (680)$ nm with the value of the numerical aperture $\text{NA} = 0.7$ from the objective lens and 780 nm of wavelength.

The light experiences change in polarization by MOKE upon reflection to have slightly elliptical polarization with the major axis rotated by the amount of Kerr angle θ_K as explained in Chapter 1.1. Such change in polarization direction could be detected by change in intensity with the aid of analyzer (Thorlabs, WP10), which differentiates the beam paths of the two beams based on the polarization direction horizontal or perpendicular to its major axis. The signal from the balanced detector

(Newfocus, 2307) is obtained by subtracting two signals from each photodiode. The resulting signal has high SNR due to the cancellation of the identical optical noise from each photodiode and high responsivity of the silicon-based photodiode in the long wavelength region around 780 nm. The optical intensity from the balanced detector could be converted to the digital data by DAQ card (National Instruments, PCI-6143) with maximum sampling rate of 250 kHz and resolution of 150 μ V.

The scanning MOKE microscope could scan the surface of the sample by using XY motorized linear stages (Newport, GTS070, GTS150) with controller unit (Newport, ESP300). Measuring MOKE signal from the nanostructured sample as well as precise measurement of the displacement could be achieved by position control of XY stage with 100 nm incremental step. Focusing of the objective lens is achieved by obtaining the position of maximum optical signal from balanced detector with one of the photodiode blocked. Automated focusing is realized by using linear motor (Thorlabs, Z812B) and control cube (Thorlabs, TDC001) with submicron resolution.

The setup has 2-axis electromagnets with in-plane and out-of plane direction with maximum magnetic field of 200 mT and 56 mT, respectively. The electromagnet is operated with bipolar power supplies (KEPCO, BOP 50-4M) with current control by applied voltage from DAQ card (National Instruments, PCI-6711). To prevent

overheating of the electromagnet, water cooling system has been adopted. A capacitor of 22 nF is utilized in parallel connection with electromagnet to reduce the high frequency fluctuation from the feedback loop in power supply.

2.1.2 Types of Measurements Available for Scanning MOKE Microscope System.

Various measurements could be realized with the scanning MOKE microscope system. Measurement of the hysteresis loop, 2D scan of the magnetic wire, domain-wall motion (DWM) measurement, and SOT-induced switching etc.

Hysteresis Loop Measurement

The most basic measurement for the scanning MOKE microscope system is hysteresis loop measurement of the sample. Hysteresis loop, often called MH loop of the sample, is MOKE signal measured with magnetic field sweep. In case of the sample with perpendicular magnetic anisotropy (PMA), polar MOKE signal is measured with out-of-plane magnetic field H_z sweep. Figure 2.1.2.1 shows hysteresis loop of the 1.5-nm Ta/3-nm Pt/0.7-nm Co/0.6-nm Cu/5-nm W/2-nm AlOx sample with PMA. The height of the hysteresis loop comes from the Kerr

rotation angle whereas linear background signal comes from the Faraday rotation that occurs in the objective lens.

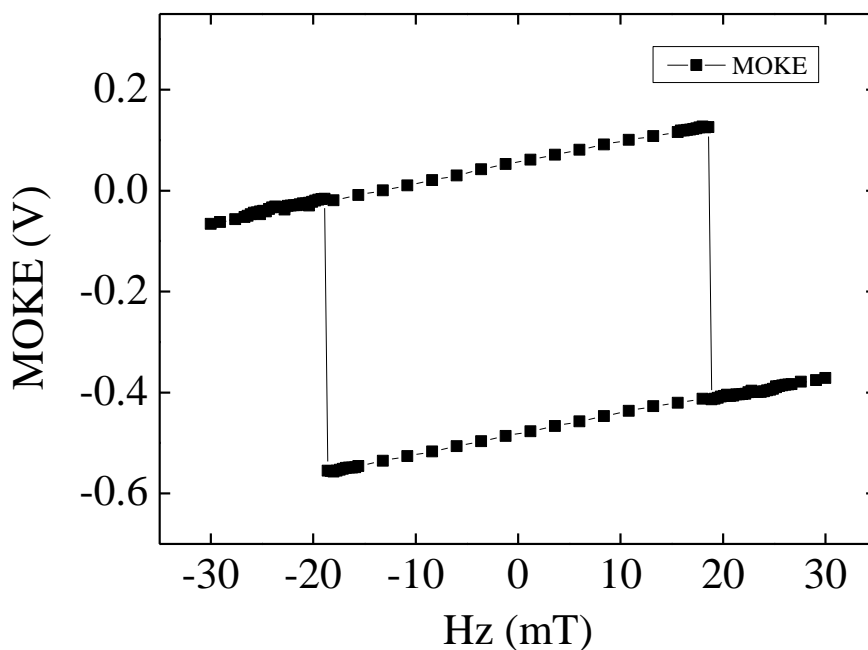


Figure 2.1.2.1 A hysteresis loop of the sample with PMA.

The process of the magnetization reversal in hysteresis loop could be separated into nucleation and expansion of the reverse domain. Such processes are affected by SOT and thus provide useful SOT quantification method with hysteresis loop measurements [44-45]. Figure 2.1.2.2 shows efficiency ϵ' for SOT-induced shift of the hysteresis loop with various in-plane magnetic field. Loopshift effect is only

visible in the longitudinal geometry, where magnetic field is along the current direction.

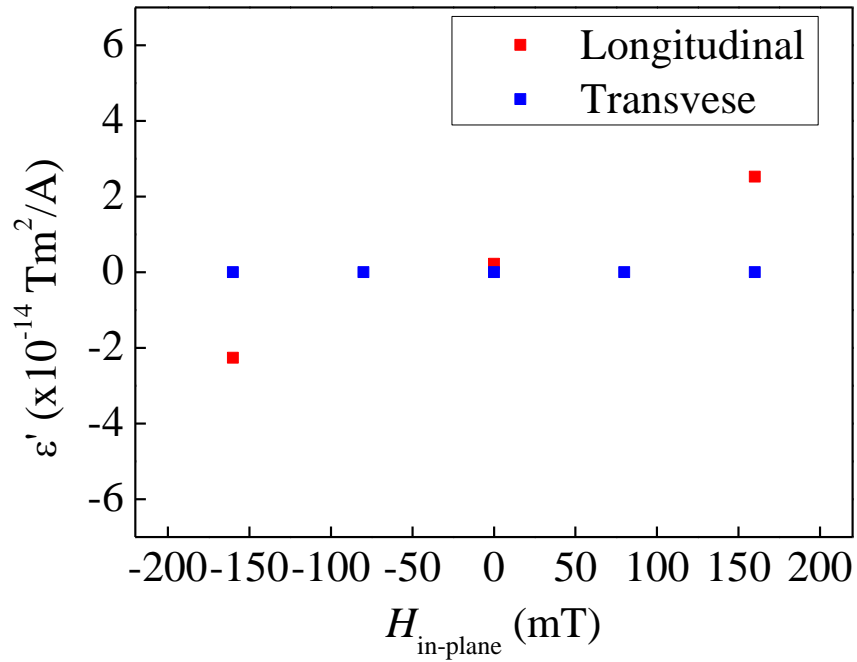


Figure 2.1.2.2 Magnitude of SOT-induced loopshift with respect to the in-plane magnetic field.

Domain-Wall Motion Measurement

Current-induced domain-wall motion (CIDWM) has drawn great attention due to the possibility for DW-based spintronic memory devices such as racetrack memory [1-6]. Spin-torques such as STT and SOT provide driving force for a DWM.

2.1.3 DW Writing Methods

Domain-wall (DW) has chiral magnetic structure that is stabilized by energy terms such as exchange energy, Dzyaloshinskii-Moriya interaction energy, and magnetostatic energy. Observing the behavior of DW could reveal the physics about the energy terms listed above. Creation of the DW for scanning MOKE microscope system is one of the most troublesome process in domain-wall motion (DWM) measurements. A DW could be created by various processes such as application of Oersted field or magnetic field and the methods for DW writing are listed.

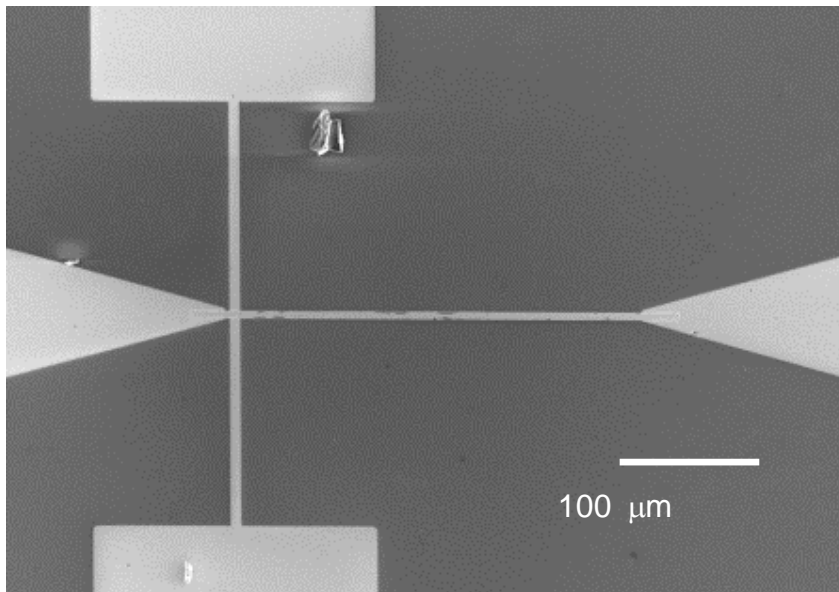


Figure 2.1.3.1 An image of magnetic wire and electrodes. The horizontal strip with bright color represents magnetic wire and other bright region represents electrodes.

Constant Magnetic Field Writing Method

Figure 2.1.3.1 shows typical structure of the magnetic wire and electrodes. A DW could be created by applying constant magnetic field to the sample. First, homogeneous magnetization state is achieved by applying saturation field H_{sat} that is larger than coercive field H_c . Then constant driving field H_d is applied until the inverted domain is detected at the observation point by real time MOKE signal analysis after its nucleation and expansion by H_d . This method is applicable only if nucleation field H_n is almost same as DW propagation field H_p . After the nucleation of the domain with applied field H_z^{ext} right above H_n , domain expands slowly since $H_z^{\text{ext}} \sim H_p$.

Field Pulse Writing Method

If H_n is much larger than H_p , created domain expands at higher speed to cover the whole sample. Since DW already passed the observation point and disappears before the detection of inverted domain is initialized, turning off the driving field

H_d upon detection of the inverted domain becomes impossible. To resolve this problem, field pulse writing method could be used.

After the initial saturation of magnetization state of the sample with H_{sat} , a magnetic field pulse H_{fp} is applied with a short period of time. The width and height of the field pulse should be adjusted. Field pulse should be strong enough to assure the nucleation of the inverted domain, meanwhile weak enough to prevent full propagation and annihilation of the DW. To lower the value of H_n , artificial nucleation site could be created by damaging the sample with localized physical, thermal, or electrical shock for film part of the patterned sample.

Oe Field Writing Method

Inverted domain can be created by Oersted field with high current. As shown in Figure 2.1.3.1, high current density J flows in the vertical writing line electrode. The current creates Oersted field to invert the magnetization near the writing line in the sample. To apply high current density up to $3 \times 10^{12} A/m^2$, short pulse with order of nanosecond is required to prevent damage in electrodes from Joule heating. High frequency pulse generator from AVTECH is used to apply short current pulse with high voltage (< 100 V) and short time width (< 1 ns)

Thermomagnetic Writing Method

At finite temperature, creation of the inverted domain at the nucleation site involves thermal assist in overcoming the energy barrier E_B for magnetization inversion since the probability for magnetization inversion follows the Arrhenius law ($P \propto e^{-E_b/k_B T}$). Therefore, providing additional thermal energy to the system helps the DW writing process by focusing an intense laser beam on a magnetic sample.

2.2 Harmonic Measurement Setup

Harmonic measurement is a widely used method for SOT quantification. Harmonic measurement measures harmonic signals $A_{1\omega}$ and $A_{1\omega}$ that are generated by sinusoidal current applied to the sample. From these amplitudes, dynamics of magnetization by SOT could be analyzed. A setup for electrical harmonic measurement method as well as optical harmonic measurement method have been demonstrated for exact quantification of SOT in various systems.

2.2.1 Setup specification

Figure 2.2.1.1 shows an image and a schematic diagram of the harmonic measurement setup with electromagnet and optical system for MOKE measurement. For optical harmonic measurement in SOT quantification, a continuous wave diode laser with center wavelength of 660 nm (Newport, LQC660-110C) has been used. The optical power of the incident probing laser ranges from 500 μW to 1.5 mW. The intensity is limited to prevent laser-induced

thermal demagnetization for the sample with thin ferromagnetic layer near $t_{co} \sim 0.3$ nm.

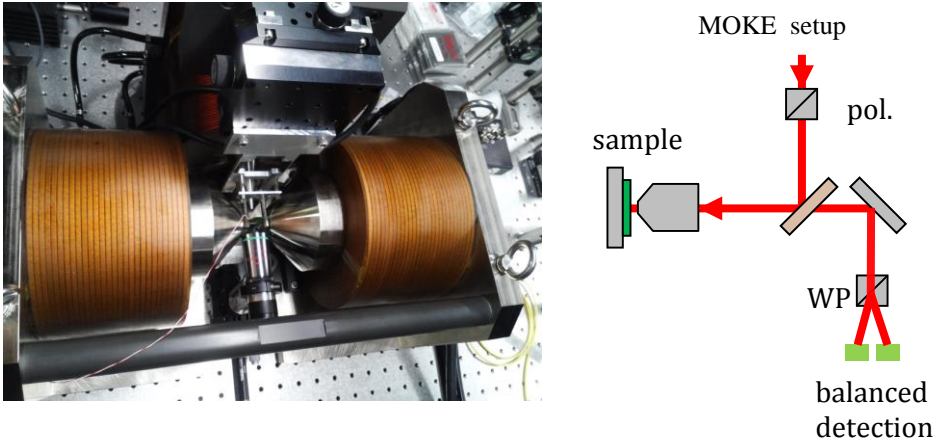


Figure 2.2.1.1 An image and a schematic diagram of the harmonic measurement setup with electromagnet and optical system for MOKE measurement.

Similar to the scanning MOKE microscope system in chapter 2.1, detection of the polarization rotation by out-of-plane magnetization is measured by balanced detector (Newfocus, 2107) with an analyzer (Thorlabs, WP10-B). The optical signal from the balanced detector is measured by DAQ card (National Instruments, PCI-6143) with maximum sampling rate of 250 kHz and resolution of $150 \mu\text{V}$. The electrical harmonic measurement is realized by adopting DAQ card with nV resolution (National Instruments, PCI-4461) to the system.

The setup for harmonic measurement is equipped with XY motorized linear stages (Newport, M-VP25-XL) with controller unit (Newport, ESP300) since samples for optical SOT harmonic measurement has microwire structure. The electromagnet system consists of 2-axis (in-plane and out-of-plane) with maximum magnetic field of 800 mT and 150 mT, respectively. The electromagnet is operated with bipolar power supplies (KEPCO, BOP 50-4M and PowerTM, PTDP-20-50) with current control by applied voltage from DAQ card (National Instruments, PCI-6711) and GPIB control, respectively. The electromagnet is made of hollow conductors, which maximizes cooling efficiency to dissipate energy from Joule heating up to 1 kW.

2.2.2 Improvements of Harmonic Measurement Setup

The optical harmonic measurement method for SOT that was previously developed [23] has been improved to give results with better signal-to-noise ratio (SNR). The improvements on the harmonic measurement setup consist of 5 major parts; extended analysis model, current shape and triggering, electromagnet modification, SNR improvements with noise reduction, and polarization control with motorized rotation mount.

Extended Analysis Model

Analysis of the harmonic measurement in SOT quantification process can be separated into two parts; one for magnetization dynamics and one for obtained signal by electrical or optical measurement. The analysis of the magnetization under SOT could be achieved by solving Landau-Lifshitz-Gilbert (LLG) equation with SOT terms. LLG equation with SOT terms is given by

$$\frac{\partial \hat{m}}{\partial t} = -\gamma \hat{m} \times (\vec{H}_{\text{ext}} + \vec{H}_{\text{ani}} + \vec{H}_{\text{SOT}}) + \alpha \hat{m} \times \frac{\partial \hat{m}}{\partial t}, \quad (2.1)$$

where α is the Gilbert damping constant; \hat{m} , a unit vector in the magnetization direction; $\vec{H}_{\text{ext}} (= H_x \hat{x} + H_y \hat{y} + H_z \hat{z})$, the external magnetic field; $\vec{H}_{\text{ani}} (= H_K^{\text{eff}} m_z \hat{z})$, the effective anisotropy field; and $\vec{H}_{\text{SOT}} (= H_T \hat{y} + H_L \hat{m} \times \hat{y})$, the SOT-induced effective field with transverse and longitudinal components. With stabilized state under SOT, $\frac{\partial \hat{m}}{\partial t} = 0$ and Eq. (2.1) expressed in spherical coordinates with $\hat{m} = (\sin\theta\cos\phi, \sin\theta\sin\phi, \cos\theta)$ becomes

$$\hat{\theta} : (H_y + H_T)\cos\phi - (H_x + H_L\cos\theta)\sin\phi = 0, \quad (2.2)$$

$$\hat{\phi} : (H_x\cos\theta + H_L)\cos\phi + (H_y + H_T)\cos\theta\sin\phi = (H_z + H_K^{\text{eff}}\cos\theta)\sin\theta.$$

(2.3)

By solving Eqs. (2.2) and (2.3) for θ and ϕ , the magnetization dynamics under SOT can be analyzed. In ref. [23], small θ assumption has been adopted to give

$$\cos\theta = 1 - \frac{(H_x+H_L)^2+(H_y+H_T)^2}{2(H_K^{\text{eff}}+H_z)^2}. \quad \text{This model has been extended by using}$$

assumption of $\theta = \theta_0 + \Delta\theta$ with small $\Delta\theta$. Solving Eqs. (2.2) and (2.3) with small $\Delta\theta$ assumption gives

$$\Delta\theta \sim \frac{H_T \cos\theta_0 \sin\phi_0 + H_L \cos\phi_0}{H_K^{\text{eff}} \cos 2\theta_0 + H_z \cos\theta_0 + H_{\text{in-plane}} \sin\theta_0} J, \quad (2.4)$$

where θ_0 and ϕ_0 are polar and azimuthal angle of the magnetization that are determined by out-of-plane and in-plane external magnetic fields H_z and $H_{\text{in-plane}}$ and anisotropy field with no current applied to the sample. In longitudinal geometry with $H_y = 0$ and $H_x \neq 0$, measured MOKE signal to the second order in J that is proportional to $m_z (= \cos\theta)$ becomes

$$\cos\theta \cong \cos\theta_0 - \frac{\beta_L}{A} \sin\theta_0 J - \left[\frac{\cos\theta_0}{2} \left(\frac{\beta_L}{A} \right)^2 + \frac{\cos\theta_0 \beta_T^2}{2H_{\text{in-plane}} A} \sin\theta_0 \right] J^2, \quad (2.5)$$

whereas the signal in transverse geometry with $H_x = 0$ and $H_y \neq 0$ becomes

$$\cos\theta \cong \cos\theta_0 - \frac{\beta_T \cos\theta_0}{A} \sin\theta_0 J - \left[\frac{\cos\theta_0}{2} \left(\frac{\beta_T \cos\theta_0}{A} \right)^2 + \frac{\cos\theta_0}{2A} \left[-\frac{2 \sin^2 \theta_0 \beta_T^2}{A} + \frac{\sin\theta_0 \beta_L^2}{H_{\text{in-plane}}} (1 + \sin^2 \theta_0) \right] \right] J^2, \quad (2.6)$$

where $A = H_K^{\text{eff}} \cos 2\theta_0 + H_z \cos \theta_0 + H_{\text{in-plane}} \sin \theta_0 = H_K^{\text{eff}} \cos^2 \theta_0 + \frac{H_z}{\cos \theta_0}$.

With less assumption applied to the analysis model in SOT measurement, investigation of the SOT for broader range in θ enabled angle dependence study of the SOT.

Current Shape and Triggering

In the early stage of development in optical harmonic measurement method, sinusoidal current has been applied to generated SOT-induced oscillation for magnetization. The shape of the current has been changed from sinusoidal form to step-sine shape in Figure 2.2.2.1 to exclude Joule heating effect from the result. The step-sine shape current consists of pairs of alternating sign and same magnitude. The differences of signal from each pair of currents in first half part make a period of sinusoidal wave, and remaining part is a duplicate of the first half part with sign inversion to average the possible thermal effect when magnitude of the current changes.

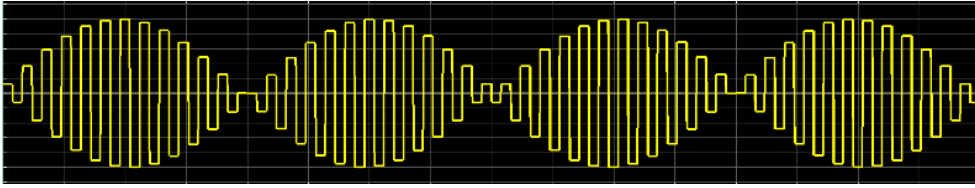


Figure 2.2.2.1 Step-sine shape of the applied current.

The complex shape of the current demands synchronization of the measured optical signal with the current applied to the sample. The synchronization was achieved by keeping or discarding data after checking the measured signal of optical signal and the current with measuring time efficiency of 30%. The synchronization process improved by analyzing synchronization between optical signal and the current after the measurement (i.e. post-triggering) that leads to reduction of time loss in measurement process.

Electromagnet Modification

The electromagnet is modified to enhance the cooling efficiency for stronger magnetic field. The resultant maximum magnetic field increased from 500 mT to 800 mT. The electromagnet is then calibrated with 3D interpolation of 2-axis magnetic fields H_x and H_z with respect to applied currents I_x and I_z as shown

in Figure 2.2.2.2. The decrease of out-of-plane field H_z seen in high I_x regime is due to the cross-talk between two cores of electromagnets.

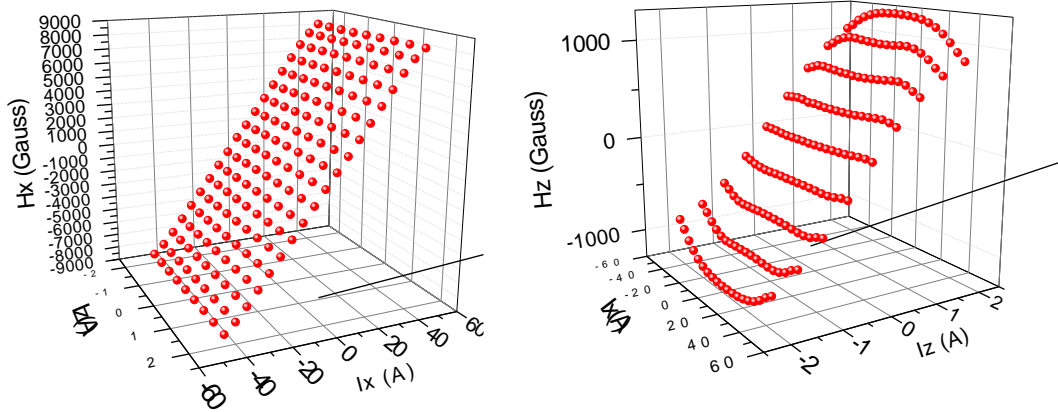


Figure 2.2.2.2 3D calibration data for 2-axis magnetic fields H_x and H_z with respect to applied currents I_x and I_z . The curvature seen in H_z plot is due to the cross-talk between two cores of electromagnets.

SNR Improvement by Noise Reduction

Signals from small oscillation of magnetization in harmonic measurement system is smaller in three or four orders of magnitude compared to the full signal from $\pm m_z$. Therefore additional methods such as lock-in technique have been utilized to attain high SNR. The SNR of the harmonic measurement system has been improved by eliminating the noise sources.

Introduction of UPS system

First, a system of uninterruptible power supply (UPS) has been introduced to electrically isolate the measurement system from other electronic apparatus. For comparison of noise level before and after the installation of UPS system, optical signal is obtained with highest sampling rate (250 kHz). The data array of measured optical signal is processed to give fast Fourier transform (FFT) spectrum result of the optical measurement system. Figure 2.2.2.3 represents noise profile of the system before and after UPS installation in FFT intensity – frequency plot. Decrease of the $1/f$ noise in low frequency and elimination of the peaks of 29.7, 77.8, 155.7, and 310.9 Hz could be seen as the effect of UPS system via electrical isolation.

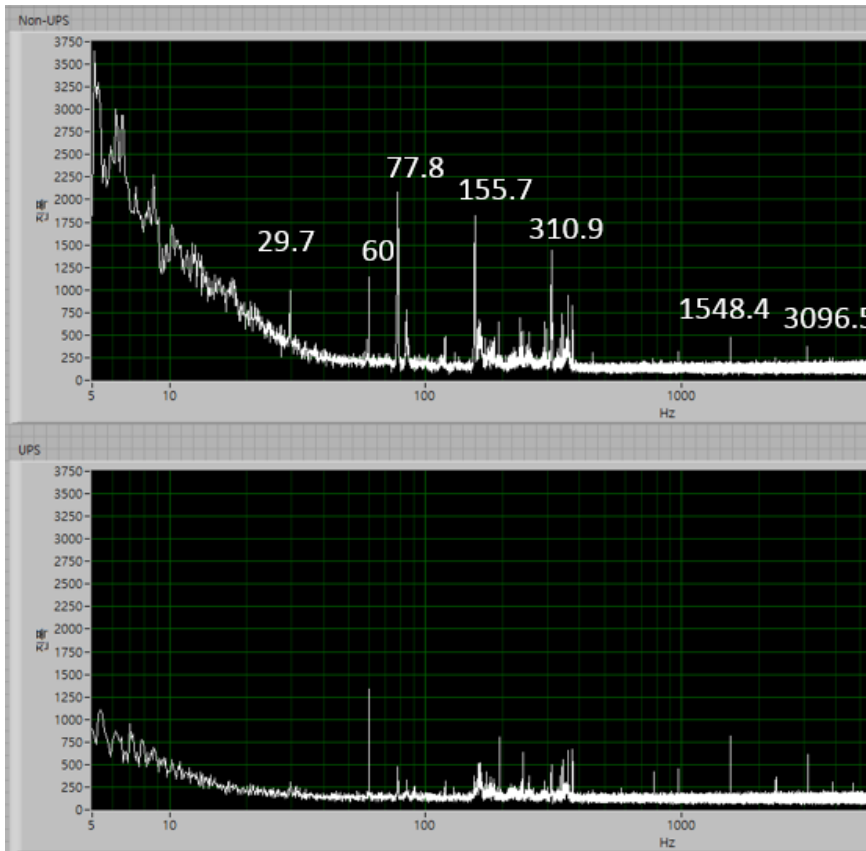


Figure 2.2.2.3 FFT noise profile before and after the installation of UPS system with respect to frequency.

Introduction of Faraday Isolator

Faraday isolator is an optical component that prevents back propagation of the reflected light. It consists of Faraday rotation part and two polarizers with their axis rotated by 45 degree. Light could pass the isolator when travels in the desired direction, however light is blocked when travels in the opposite direction.

Therefore, optical feedback to the laser diode is eliminated and thus, stability of the laser intensity could be increased. The Faraday isolator has been installed and noise profiles before and after the installation are shown in Figure 2.2.2.4. As seen in Figure 2.2.2.4, drastic decrease of the noise level more than 10 times has been achieved by using Faraday isolator to the optical MOKE measurement system.

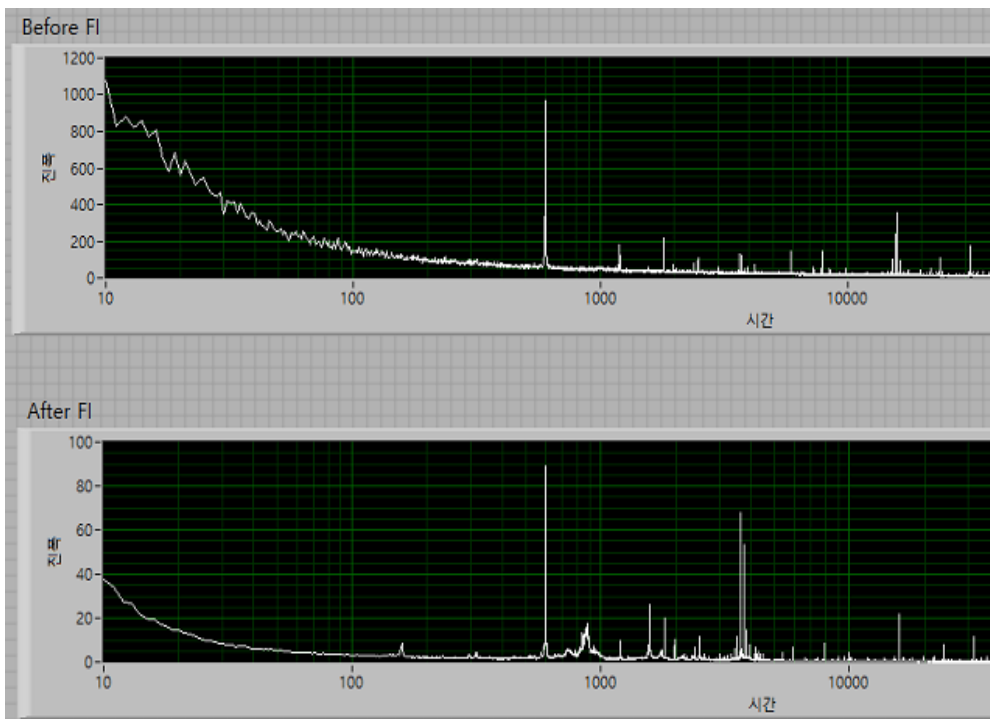


Figure 2.2.2.4 FFT noise profile before and after installation of the Faraday isolator. The x-axis has unit of 0.1 Hz in this plot.

Selection of the Laser

To improve the SNR of the system, noise characteristics of a HeNe laser (Newport, HNL210L-EC) and a diode laser (Newport LQC660-110C) have been compared. Figure 2.2.2.5 shows noise profile of the MOKE measurement system with a HeNe laser and a diode laser. Diode laser has stable output power whereas HeNe laser has stable center wavelength due to the fixed energy levels of the He and Ne gas atoms.

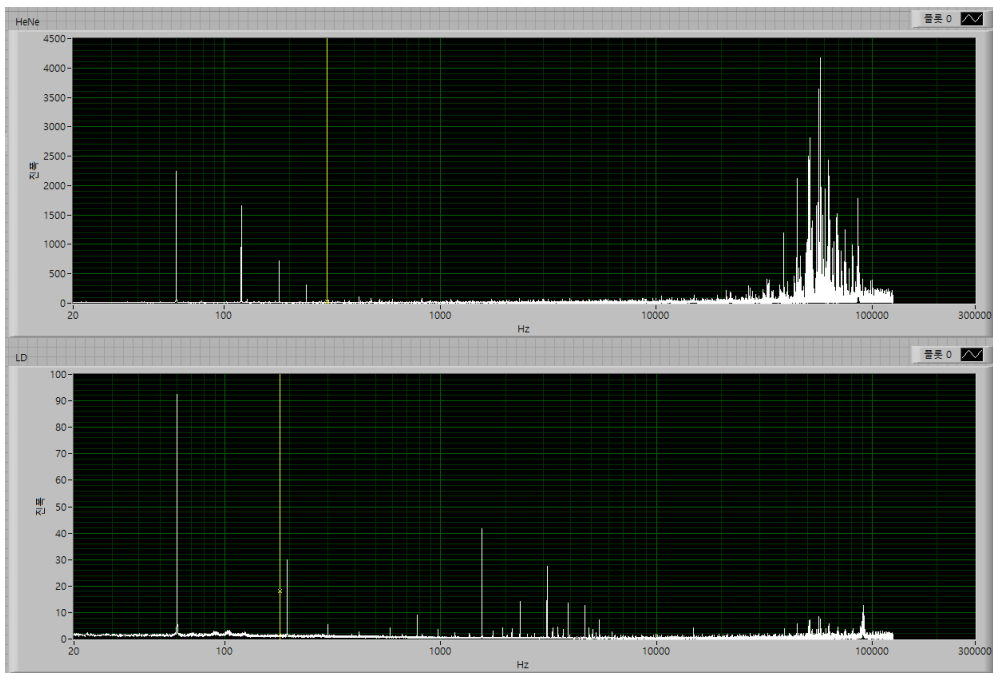


Figure 2.2.2.5 FFT noise profiles of a HeNe laser and a diode laser.

Polarization Control with Motorized Rotation Mount

Control of the polarization state of light is a unique feature in magneto-optic measurements compared with magneto-transport measurements. Polarization state of light can be manipulated by linear polarizers and passive/active retarders such as quarter-wave plates (QWP), half-wave plates (HWP), and photo-elastic modulations (PEM). Figure 2.2.2.6 shows plot of the intensity of linear polarization with respect to analyzer angle. Maximum intensity at angle of 135, 315 degrees and minimum intensity at 45, 225 degrees represents linear polarization with its polarization direction marked with black arrows.

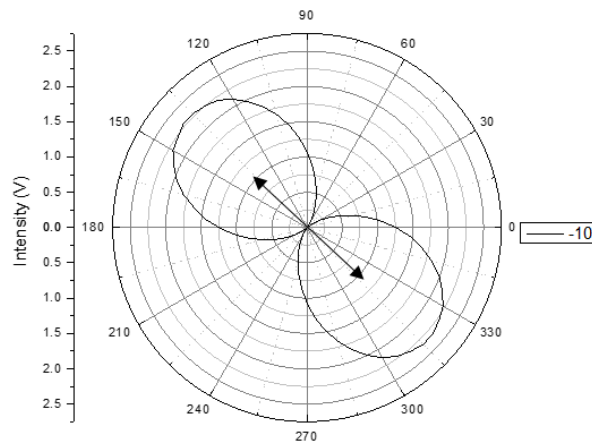


Figure 2.2.2.6 Polar plot of the intensity with respect to the analyzer angle for linear polarization.

HWP inverts the direction of the polarization with respect to its major axis. Therefore, rotation of HWP with initial linear polarization generates rotation of the polarization of the final polarization. Figure 2.2.2.7 shows rotation of the polarization direction with rotating HWP angle. The ratio of the actual rotation angle of the polarization to the HWP rotation angle was extracted from the angle with maximum intensity to be 1.99993 that agrees with the literature value of 2.

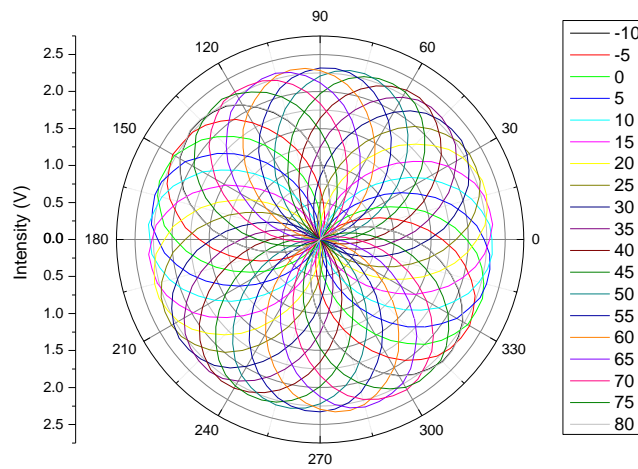


Figure 2.2.2.7 Polar plot of the intensity with respect to the analyzer angle for linear polarization with various HWP rotation angles.

Chapter 3

Comparison between spin-orbit torques measured by domain-wall motions and harmonic measurements

Spin-orbit torque measurement methods have been proposed with various physical configurations. Different values of SOT measured in different configurations such as domain-wall motions, harmonic measurements required cross-validation and conversion factor between results of those methods needs to be verified. In this chapter, results from three different SOT measurement scheme based on two different phenomena have been compared to check the compatibility between the three measurement schemes.

3.1 Introduction

Current control of the magnetization has been of great interest due to the academic curiosities as well as the application opportunities toward spintronic devices. For current control of the magnetization, spin-orbit torque (SOT) from strong spin-orbit coupling in heterostructures such as heavy-metal/ferromagnetic (HM/FM) stacks has been studied intensively [41-42]. The SOT plays a decisive role in various phenomena such as current-driven magnetization switching and current-induced domain-wall (DW) motion. To quantify the SOT in the current-driven magnetization switching, either electric [18, 20, 24-25] or optical [26, 45] harmonic measurement technique has been proposed and widely utilized. For the current-induced DW motion, the SOT is quantified in configuration of either depinning [47-48] or creeping [49] motion of the DW. The proportionality with a proportionality constant $\pi/2$ between the spin torque efficiencies measured from the DW motion and harmonic measurements has been suggested theoretically [12] and verified experimentally [27] for the case of Ta/CoFeB/MgO. Here we adopt these measurement schemes for analysis of the SOTs in several different HM/FM heterostructures to check the compatibility as well as the relationship among the schemes.

3.2 Experimental Details

For this study, samples were prepared with various stacks of 5-nm Ta/2.5-nm Pt/0.9-nm Co/2.5-nm X/1.5-nm Pt with different X (= Pt, Ta, Ti, Al, Au, Pd and Ru, 7 materials). These materials exhibit various spin Hall angle θ_{Hall} that could affect the sign and magnitude of SOT. The bottom Ta layer is used for better crystallinity and adhesion. The top Pt layer is employed to prevent the contamination and/or oxidation. The films were sputtered on the top of diced Si/SiO₂ wafer of 12×12 mm² in size. The base pressure of the sputtering chamber was kept lower than 5×10^{-8} Torr and the working pressure was set to 2 mTorr during deposition. After deposition, the films were patterned into microstrips by optical lithography and Ar milling. Then, 5-nm Ti/100-nm Au electrodes were deposited onto the microstrips for injection of current.

All samples exhibit perpendicular magnetic anisotropy (PMA). The effective anisotropy fields H_K were extracted from the hard axis loop measured by a vibrating sample magnetometer (VSM). Then the SOT efficiency was characterized either by the two different measurement schemes based on domain-wall (DW) motion or by the harmonic signal measurement. For the DW measurement schemes, the current density was kept lower than 1.6×10^{10} A/m² to prevent the Joule heating effect. For harmonic measurement schemes, the current density was kept lower than 4.5×10^{10} A/m².

3.3 Measurement of SOT in DWM

For the DW-based measurement, two different types of the measurement schemes were employed, originally proposed by Emori *et al* [48] and Je *et al* [49], respectively. The former is sensitive to the DW depinning characteristics at local pinning sites, while the latter measures the average speed of the creep DW motion. To check the compatibility between these two schemes, we adopted both the schemes to measure the SOT efficiencies on the same area of the microstrips.

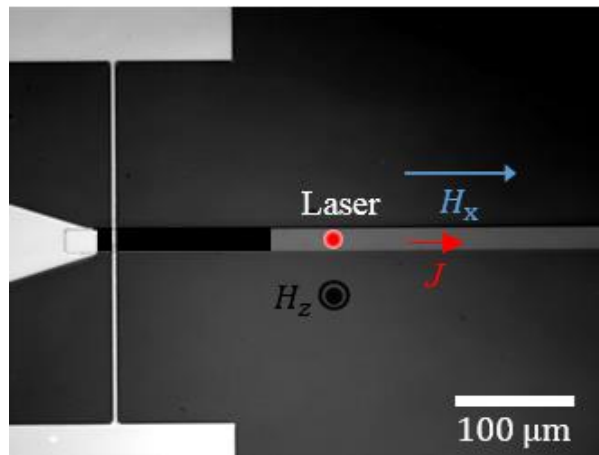


Figure 3.3.1 Schematic drawing of measurement setup with microscope image microstrip (black and grey areas) with electrodes (white areas). The black and grey areas depict opposite domains in the magnetic strip, respectively. The arrows indicate the directions and polarities of H_x , H_z , and J , respectively.

Figure 3.3.1 shows the schematic diagram of these measurement schemes. For both experiments, a DW is initially create, the DW motion is detected by the MOKE probe. For the former (depinning) scheme, the position of the MOKE probe is placed close ($<20\ \mu\text{m}$) to the initial DW and then, the DW depinning field is measured with sweeping the out-of-plane magnetic field H_z . On the other hand, for the latter (creeping) scheme, the position of the MOKE probe is placed far ($>50\ \mu\text{m}$) away from the initial DW and then, the DW arrival time to the probing spot is measured. Therefore, the former provides a direct measure of the depinning characteristics, whereas the latter measures the DW creeping speed.

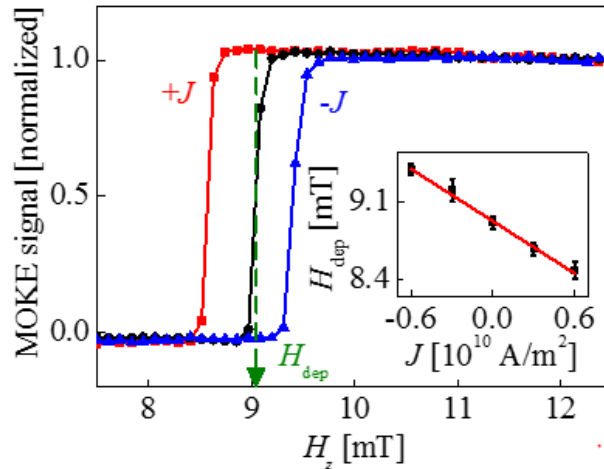


Figure 3.3.2 Plot of the MOKE signal with respect to H_z under constant current biases $-J$ (blue), 0 (black), and $+J$ (red) with $J = 0.6 \times 10^{10}\ \text{A/m}^2$. The green vertical arrow indicates H_{dep} . (inset) Plot of H_{dep} with respect to J .

Figure 3.3.2 plots the MOKE signal with respect to H_z measured by the

former scheme for the sample with $X = \text{Ti}$ with different polarities of the current biases as denoted inside the plot. The abrupt change in the MOKE signal indicates the passage of the DW across the probing spot and thus, the depinning field H_{dep} can be measured as designated by the green arrow inside the plot. It is clear from the plot that H_{dep} is sensitive to the current biases. From the linear dependence of H_{dep} with respect to the applied current density J as shown by the inset of Figure 3.3.2, one can estimate the SOT efficiency $\varepsilon_{\text{DW}}^{(1)}$ for the current-to-field conversion as $\varepsilon_{\text{DW}}^{(1)} = -\partial H_{\text{dep}}/\partial J$.

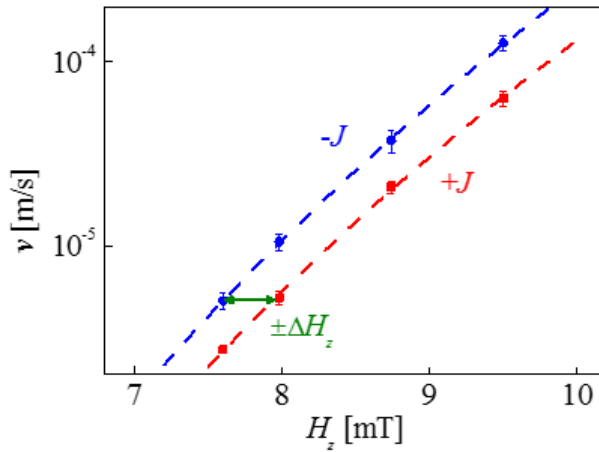


Figure 3.3.3 Plot of v with respect to H_z under current biases $-J$ (blue) and $+J$ (red) with $J = 0.2 \times 10^{10} \text{ A/m}^2$. The green horizontal arrow shows ΔH_z .

On the other hand, Figure 3.3.3 plots the DW speed v with respect to H_z measured by the latter scheme for the same sample with different polarities of

the current biases. All the ν curves exhibit the same behavior except the horizontal shifts ΔH_z caused by the different current bias as denoted inside the plot. From the linear dependence between ΔH_z and J , one can again measure the SOT efficiency $\varepsilon_{\text{DW}}^{(2)}$ as $\varepsilon_{\text{DW}}^{(2)} = \Delta H_z/2J$.

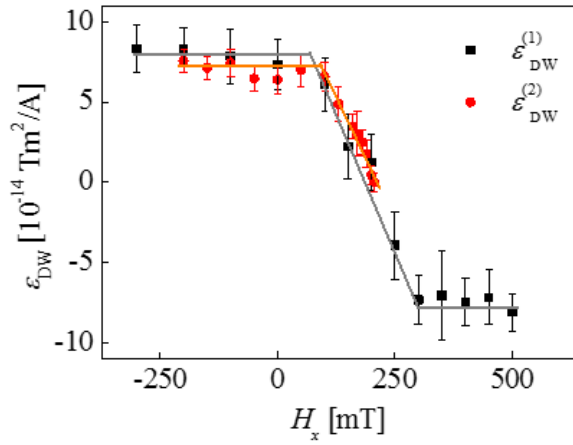


Figure 3.3.4 Plot of $\varepsilon_{\text{DW}}^{(1)}$ (black) and $\varepsilon_{\text{DW}}^{(2)}$ (red) with respect to H_x .

The results from these two measurement schemes are summarized by Figure 3.3.4 as the plots of $\varepsilon_{\text{DW}}^{(1)}$ and $\varepsilon_{\text{DW}}^{(2)}$ with respect to the in-plane magnetic field H_x , respectively. It is clear that both the results from the two schemes show basically the same behavior. The minor discrepancy is possibly ascribed to the stochastic errors, which are inevitable in the present thermal activation phenomena. Therefore, one can conclude that both schemes can be used to measure the SOT

efficiency of the DW motion. The shape of $\varepsilon_{\text{DW}} - H_x$ follows the typical behavior of the SOT-induced phenomena with two saturated regimes and a transition regime in-between. For this case, ε_{DW} is given by the relation $\varepsilon_{\text{DW}}(H_x) = \varepsilon_{\text{DW}}^{\text{sat}}(\hat{z} \cdot (\hat{m}_{\text{DW}}(H_x) \times \hat{y}))$, where $\varepsilon_{\text{DW}}^{\text{sat}}$ is the maximum value of ε_{DW} when the magnetization \hat{m}_{DW} inside the DW is fully saturated along the x axis forming Néel-type DW. The measured values of $\varepsilon_{\text{DW}}^{\text{sat}}$ are summarized in Figure 3.3.5 for the samples Pt/Co/X with different materials X.

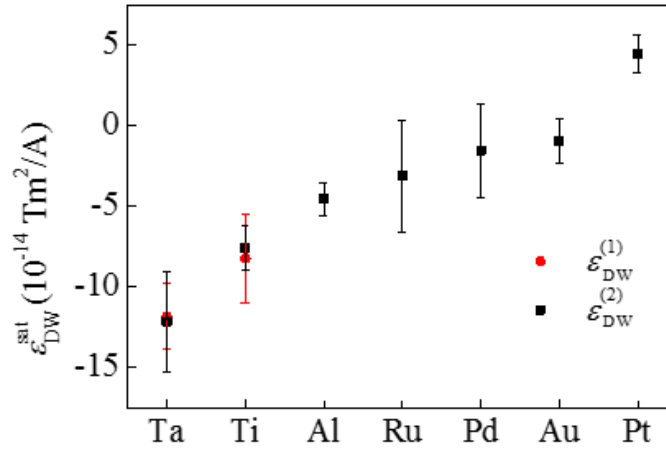


Figure 3.3.5 Plot of $\varepsilon_{\text{DW}}^{\text{sat}}$ for Pt/Co/X stacks.

3.4 Measurement of SOT in HM

The present SOT efficiencies of the DW motion are then compared with the SOT efficiency from the harmonic signal measurement. For the harmonic signal measurement, the uniform magnetization state without any DW is characterized. By applying an small external magnetic field bias (H_x, H_y, H_z) , the magnetization is tilted to a polar angle θ_0 with $\cos \theta_0 = 1 - \frac{1}{2}(H_x^2 + H_y^2)/(H_K + H_z)^2$. If one injects an alternating current of sinusoidal profile $J = J_0 \sin \omega t$ to the present situation, where J_0 is the maximum amplitude and ω is the angular frequency, the current-induced SOT generates further deviation of the magnetization angle θ , resulting in

$$\cos \theta = \cos \theta_0 + A_{1\omega} \sin \omega t + A_{2\omega} \sin^2 \omega t, \quad (3.1)$$

with

$$A_{1\omega} = -J_0 \frac{\varepsilon_L H_x + \varepsilon_T H_y}{(H_K + H_z)^2}, \quad (3.2)$$

and

$$A_{2\omega} = -J_0^2 \frac{\varepsilon_L^2 + \varepsilon_T^2}{2(H_K + H_z)^2}, \quad (3.3)$$

where ε_L and ε_T are the longitudinal and transverse SOT efficiency for current-

to-field conversion.

In optical measurement, one can directly detect $\cos \theta$, since the polar MOKE signal is proportional to the z component of the magnetization m_z i.e. $\cos \theta$. Then, for the longitudinal setup with $H_x \neq 0$, $H_y = 0$, and $H_z = 0$, one can easily extract ε_L by subtracting the two polar MOKE signals measured with $\pm J$, where the subtracted polar MOKE signal Δm_z ($\equiv m_z(J) - m_z(-J)$) can be written as $\Delta m_z = \Delta m_z^{\max} \sin \omega t$ with $\Delta m_z^{\max} = 2J_0 \varepsilon_L (H_x / H_K^2)$. It is worthwhile to note that the present procedure eliminates the Joule heating effect, which exhibits $\sin^2 \omega t$ dependence.

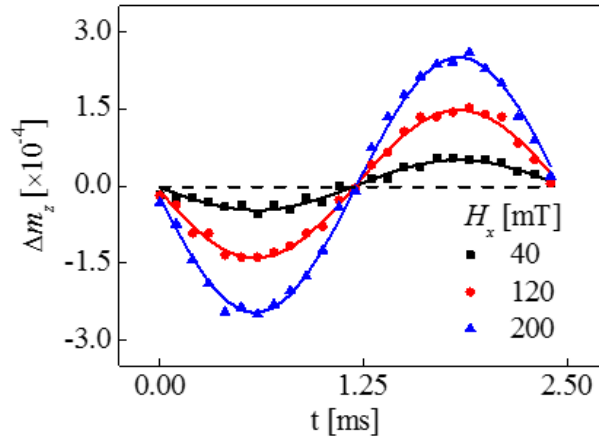


Figure 3.4.1 Plot of Δm_z with respect to t for several different H_x 's as denoted inside the plot. (b) Plot of Δm_z^{\max} with respect to H_x . The red line shows the best linear fitting. (b) Plot of ε_L for Pt/Co/X stacks.

Figure 3.4.1 plots the measured Δm_z with respect to time t for several different H_x as denoted inside the plot, where J_0 is fixed to 2.4×10^{10} A/m² and H_K is measured as 1.13 T from the VSM measurement. The clear sinusoidal behavior verifies the validity of the present measurement scheme.

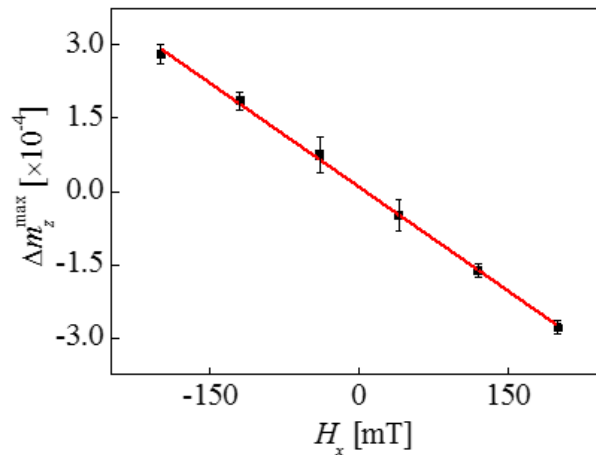


Figure 3.4.2 Plot of Δm_z^{\max} with respect to H_x . The red line shows the best linear fitting.

The amplitude Δm_z^{\max} of the sinusoidal Δm_z variation is then plotted with respect to H_x in Figure 3.4.2. From the clear linear proportionality, one can unambiguously determine the value of ε_L . The measured values of ε_L are summarized in Figure 3.4.3 for the samples Pt/Co/X with different materials X.

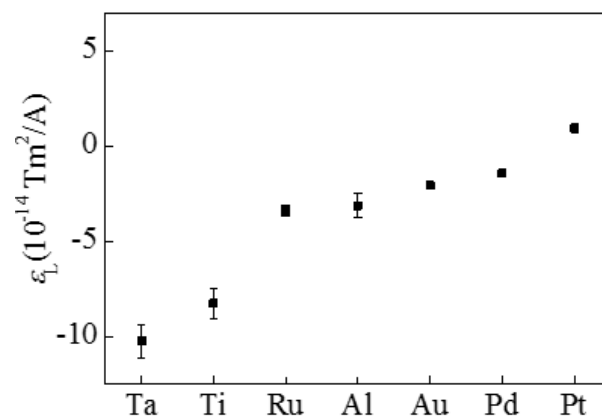


Figure 3.4.3 Plot of ϵ_L for Pt/Co/X stacks.

3.5 Comparison of SOT in DWM and HM

Finally, we compare the results between the DW-based measurement and the harmonic signal measurement. The correlation between $\varepsilon_{\text{DW}}^{\text{sat}}$ and ε_{L} is plotted in Figure 3.5.1 for the samples Pt/Co/X with different materials X. The red line shows the proportionality with the proportionality constant $(\pi/2)$, i.e. $\varepsilon_{\text{DW}}^{\text{sat}} = (\pi/2)\varepsilon_{\text{L}}$, where the proportionality constant comes from the integration over the DW profile [12, 27]. The plot shows that $\varepsilon_{\text{DW}}^{\text{sat}}$ and ε_{L} roughly follow the proportionality relation with maximum deviation of about 30% for stacks with X = Ta and Ti. Such deviation might be attributed to the effects from the domain canting and/or transverse SOT, as discussed below.

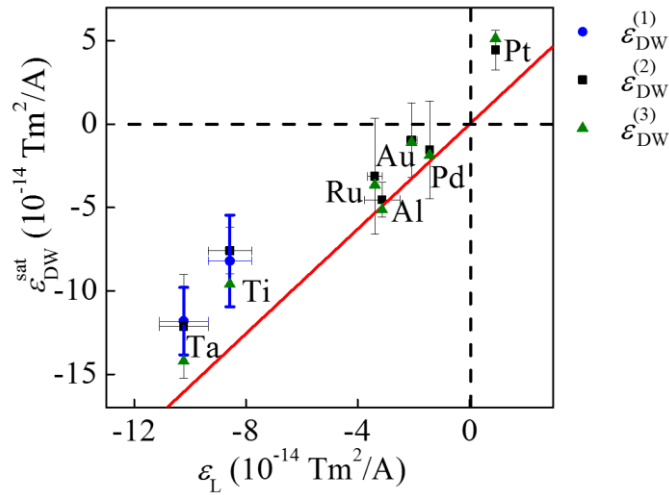


Figure 3.5.1 Plot of $\varepsilon_{\text{DW}}^{\text{sat}}$ with respect to ε_{L} for Pt/Co/X stacks with X = Ta, Ti, Al, Ru, Pd, Au, and Pt. The blue, black, and green symbols corresponds to $\varepsilon_{\text{DW}}^{(1)}$, $\varepsilon_{\text{DW}}^{(2)}$, and $\varepsilon_{\text{DW}}^{(3)}$, respectively. The red line shows the $\pi/2$ proportionality.

Under application of a large in-plane field H_x , the magnetization inside the domain is canted. According to Ref. [48], such canting effect modifies the SOT efficiency by factor of α as

$$\varepsilon_{\text{DW}}/\varepsilon_{\text{DW}}^0 \equiv \alpha = \frac{2H_{\text{K}}}{\sqrt{H_{\text{K}}^2 - H_x^2}} \tan^{-1} \left(\frac{H_{\text{K}} - H_x}{\sqrt{H_{\text{K}}^2 - H_x^2}} \right) \cos \varphi, \quad (3.4)$$

where $\varepsilon_{\text{DW}}^0$ denotes the value without considering the canting effect and φ is the azimuthal angle of magnetization inside the DW. By use of the experimental values of H_{K} and H_x , the present effect is estimated to reduce $\varepsilon_{\text{DW}}^{\text{sat}}$ by about 20% in maximum for the stack with X = Ti. Therefore, the large portion of the discrepancy is possibly attributed to the magnetization canting effect. The green symbols in Figure 3.5.1 show $\varepsilon_{\text{DW}}^{(3)} = \varepsilon_{\text{DW}}^{(2)}/\alpha$ after correction of the canting effect.

The transverse SOT also possibly reduces $\varepsilon_{\text{DW}}^{\text{sat}}$, since the transverse SOT prefers the Bloch-type DW configuration by rotating φ away from the Néel-type DW configuration. However, based on the experimental values, the rotation of φ due to the transverse SOT is estimated to be less than 1° , which results in less than 1% of the $\varepsilon_{\text{DW}}^{\text{sat}}$ reduction. Therefore, the effect of the transverse SOT is ignorable

in our samples.

The last possibility we like to mention is that the DW-based measurements are inevitably sensitive to the nature of the macro- and/or micro-pinning sites, since these measurements are done for either the DW depinning or creeping motions. Therefore, it might be possible that the DW-based measurement results are inherently different from the harmonic signal measurement results, since the harmonic signal measurement is done for the coherent magnetization rotation that is less sensitive to the pinning characteristics. We are unable to exactly quantify the present effect, but, by comparing the experimental values with the above estimations, the present effect might be smaller than the magnetization canting effect.

3.6 Conclusion

In summary, from the measurements of the SOT efficiencies by use of three different measurement schemes for various Pt/Co/X films with X= Ta, Ti, Ru, Al, Pd, Au, and Pt (7 materials), we confirm the validities of the measurement schemes. The measurement results from two different schemes—based on either DW depinning or DW creeping—exactly coincide to each other. Also, these DW-based measurement results roughly match to the harmonic signal measurement, with proportionality constant ($\pi/2$) that comes from the DW profile. The discrepancy between the DW-based measurements and the harmonic signal measurement is mainly attributed to the magnetization canting in the domains.

Chapter 4

Development of artifact-free optical spin-orbit torque magnetometry

Quantification methods of the spin-orbit torque have been proposed. Harmonic measurement method has been widely utilized due to its accessibility. However, artifacts such as planar Hall effect and anomalous Nernst effect hinders exact quantification of SOT in the electric harmonic measurement method. Similar phenomena also occur in optical measurement method, reproducing the difficulties for SOT analysis. In this chapter, this problem is solved by utilizing polarization of the light, an additional degree of freedom for optical measurement method.

4.1 Introduction

Current control of magnetization via the spin-orbit torque (SOT) has opened a new horizon for magnetic memory devices. SOT causes magnetization switching and domain wall motion [15, 41-42, 47-49] that enable read/write operations in spintronic memory devices. For more efficient operation of such spintronic devices and further investigation of underlying SOT mechanisms, a precise and artifact-free SOT quantification method is required.

The harmonic Hall voltage measurement method is widely used for quantification of the SOT [18, 24, 32, 50]. This method measures the first and second harmonic components in the transverse voltage V_{xy} ; this mainly involves the anomalous Hall effect (AHE) signal ($V_{xy}^{AHE} \propto m_z$, where m_z is magnetization along the z-axis). Studies on SOT with various materials have identified additional artifacts with sizable V_{xy} , such as the planar Hall effect (PHE) ($V_{xy}^{PHE} \propto m_x \cdot m_y$) [20, 24, 32, 50] and anomalous Nernst effect (ANE) ($V_{xy}^{ANE} \propto \nabla T \cdot m_x$, where ∇T is the temperature gradient) [20, 51-53]. Because all these artifacts are simultaneously included in the measured harmonic signal V_{xy} ($= V_{xy}^{AHE} + V_{xy}^{PHE} + V_{xy}^{ANE}$), it is difficult to exactly quantify the magnitude of the SOT. Though several correction methods have been proposed [20, 24, 50-51], determination of the exact SOT value under some conditions remains difficult, and thus, problems in SOT

analysis with artifacts have not been completely resolved.

SOT quantification methods based on optical measurement have also been proposed [22-23, 26, 46]. The optical SOT quantification method mainly measures the polar magneto-optic Kerr effect (pMOKE) signal ($\theta_K \propto m_z$). The optical signal is reported to involve both AHE-like (pMOKE) and PHE-like (optic PHE) contributions [26, 46]. Therefore, problems similar to those related to the PHE signal might also occur in the optical measurement method. However, there is a critical difference between optical and electric measurement methods. In the electrical measurement method, both the manipulation and the detection of the magnetization state are accomplished by the same electric current. In contrast, in the optical measurement method, electric current and the magneto-optical effect are respectively used for the manipulation and the detection of the magnetization state. Moreover, the polarization state of light can be changed without affecting the magnetization state.

Manipulation of the polarization state of light provides an additional degree of freedom to resolve artifact-induced problems in SOT analysis. Thus far, vanishing of the optic PHE signal at a certain polarization angle has been reported [26, 46]. This is mainly because the pMOKE and optic PHE have different dependences on the polarization state of light, thus enabling further investigations to resolve artifact-induced problems in the optical SOT measurement method.

Here, we propose another artifact-free optical measurement method for SOT quantification. The Jones-matrix calculus enabled us to find an optical setup in which the optic PHE signal is eliminated. The optical setup includes photoelastic modulation (PEM) and balanced detection (BD), making it accessible to widely used conventional PEM setups [26, 54-58]. We demonstrated the elimination of the optic PHE signal in a metallic stack of Pt/Py bilayers.

4.2 Experimental Details

For the experiments, we prepared a magnetic sample of 1.5-nm Ta/6-nm Pt/8-nm Py/2-nm TiO₂ grown on a Si/SiO₂ substrate by a DC magnetron sputtering system. The TiO₂ capping layer was formed by natural oxidation after the deposition of a metallic 2-nm Ti layer. The film is patterned into a wire of 20- μ m width by photolithography, followed by 15-nm Ti/100-nm Au electrode deposition for current injection. The sputtering system has a base pressure of 1×10^{-8} Torr and working pressure of 3 mTorr with Ar atmosphere of 99.999% purity. In-plane and out-of-plane hysteresis loops were measured using a vibrating-sample magnetometer (VSM), and saturation magnetization of $\mu_0 M_s = 0.87$ T and effective perpendicular anisotropy field of $\mu_0 H_K^{\text{eff}} = -0.56$ T were found.

For manipulating the polarization state of light, PEM with modulation frequency of 50.078 kHz and amplitude of quarter-wave retardation was used. Then, a lock-in amplifier (LIA) was used for measuring the intensity modulated by the PEM. A diode laser with center wavelength of 660 nm was used. A balanced photoreceiver with 10-MHz bandwidth was used to properly measure harmonic signals of optically modulated signals by the PEM.

4.3 SOT Results with PEM on/off

The polarization state of light provides an additional degree of freedom in the optical SOT measurement method. To control this polarization, passive and active retarders such as half-wave plate (HWP), quarter-wave plate (QWP), and PEM were used. Various optical setups with various combinations of these retarders at several different positions and with either single or balanced detection were examined using the Jones-matrix calculus to check the possibility of elimination of the optic PHE signal. Details of the Jones calculus are described in the supplementary material. The results indicate that a setup with a PEM and BD enables us to eliminate the optic PHE signal. Figure 4.3.1 shows a schematic diagram of our optic setup. To clearly visualize the elimination of the optical PHE signal, two HWPs (HWP1 and HWP2 before the sample and detector, respectively) were added to the system.

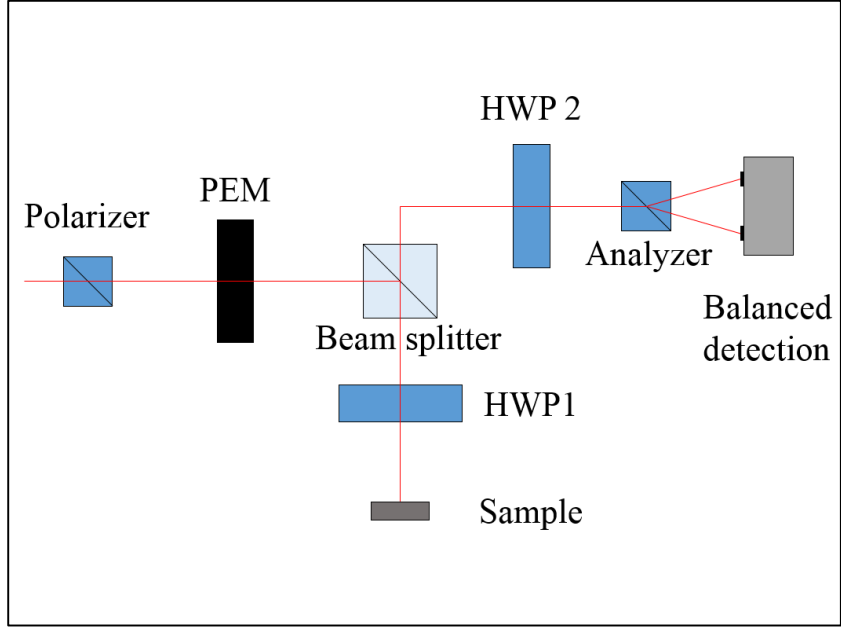


Figure 4.3.1. A schematic diagram of the optical SOT measurement setup. The setup has two operational modes depending on the PEM's state (on/off). When PEM is turned off, the measured intensity involves signals from both pMOKE and optic PHE. When PEM is turned on, the polarization of light becomes modulated and the second harmonic amplitude A_{2f} involves the signal from pMOKE only.

To explain how the setup works, we compare cases in which PEM is turned on and turned off. When PEM is turned off, the incident light on a sample has a linear polarization state. The BD signal intensity with pMOKE and optic PHE is given by

$$I_{BD}^{\text{off}} = -2\alpha_{\text{pMOKE}} \cos\theta_M - \beta_{\text{PHE}} \sin^2\theta_M \sin 2(\phi_{\text{pol}} - \phi_M), \quad (4.1)$$

where α_{MOKE} and β_{PHE} are the coefficient of the pMOKE and optic PHE, respectively. θ_{M} and ϕ_{M} are the polar and azimuthal angle of magnetization, respectively. Here, ϕ_{pol} is the angle of the polarization direction of light that can be manipulated by rotating HWP1. By injecting electric current, the SOT reorients the magnetization by $\Delta\theta_{\text{M}}$ and $\Delta\phi_{\text{M}}$. Then, the measured signal from the SOT can be written as

$$\Delta I_{\text{BD}}^{\text{off}} = 2\alpha_{\text{pMOKE}}\sin\theta_{\text{M}}^0\Delta\theta_{\text{M}} - 2\beta_{\text{PHE}}(\sin\theta_{\text{M}}^0\cos\theta_{\text{M}}^0\sin 2(\phi_{\text{pol}} - \phi_{\text{M}}^0)\Delta\theta_{\text{M}} - \sin^2\theta_{\text{M}}^0\cos 2(\phi_{\text{pol}} - \phi_{\text{M}}^0)\Delta\phi_{\text{M}}), \quad (4.2)$$

for a general magnetization configuration, where θ_{M}^0 and ϕ_{M}^0 are respectively the polar and azimuthal angle of magnetization with no current applied to the wire.

For samples with IMA where $\theta_{\text{M}}^0 = \frac{\pi}{2}$, the BD signal intensity is simplified as

$$\Delta I_{\text{BD,IMA}}^{\text{off}} = 2\alpha_{\text{pMOKE}}\Delta\theta_{\text{M}} + 2\beta_{\text{PHE}}\cos 2(\phi_{\text{pol}} - \phi_{\text{M}}^0)\Delta\phi_{\text{M}}. \quad (4.3)$$

The reorientation $\Delta\theta_M$ and $\Delta\phi_M$ of the magnetization by the SOT could be calculated by solving the Landau-Lifschitz-Gilbert (LLG) equation. With a quasistatic assumption that $\frac{\partial \hat{m}}{\partial t} = 0$, the LLG equation becomes

$$0 = \alpha \hat{m} \times (\vec{H}_{\text{ext}} + \vec{H}_{\text{ani}} + \vec{H}_{\text{SOT}}), \quad (4.4)$$

where α is the Gilbert damping constant; \hat{m} , a unit vector in the magnetization direction; $\vec{H}_{\text{ext}} (= H_x \hat{x} + H_y \hat{y} + H_z \hat{z})$, the external magnetic field; $\vec{H}_{\text{ani}} (= H_K^{\text{eff}} m_z \hat{z})$, the effective anisotropy field; and $\vec{H}_{\text{SOT}} (= H_T \hat{y} + H_L \hat{m} \times \hat{y})$, the SOT-induced effective field with transverse and longitudinal components. In the longitudinal geometry with $\vec{H}_{\text{ext}} = H_x \hat{x}$, the SOT-induced reorientation $\Delta\theta_M$ and $\Delta\phi_M$ of magnetization can be written as

$$\Delta\theta_M = \frac{H_L}{H_x \sin\theta_M^0 + H_K^{\text{eff}} \cos 2\theta_M^0}, \Delta\phi_M = \frac{H_T}{H_x}. \quad (4.5)$$

Upon combining Eqs. (4.3) and (4.5), the SOT-induced signal under the in-plane field H_x and $\phi_M^0 = 0$ becomes

$$\Delta I_{\text{BD,IMA}}^{\text{off}} = 2\alpha_{\text{pMOKE}} \frac{H_{\text{L}}}{H_{\text{x}} - H_{\text{K}}^{\text{eff}}} + 2\beta_{\text{PHE}} \cos 2(\phi_{\text{pol}}) \frac{H_{\text{T}}}{H_{\text{x}}}. \quad (4.6)$$

The first term is caused by pMOKE; it remains almost constant over the experimental range of H_{x} ($\ll -H_{\text{K}}^{\text{eff}}$), as shown in Figure 4.3.2. The second term is caused by the optic PHE; it is inversely proportional to H_{x} and can be eliminated by adjusting ϕ_{pol} , as shown in Figure 4.3.2. Note that the step-like feature at $\phi_{\text{pol}} = 45^\circ$ represents the elimination of the optic PHE signal in IMA samples, as reported by previous studies [26, 46].

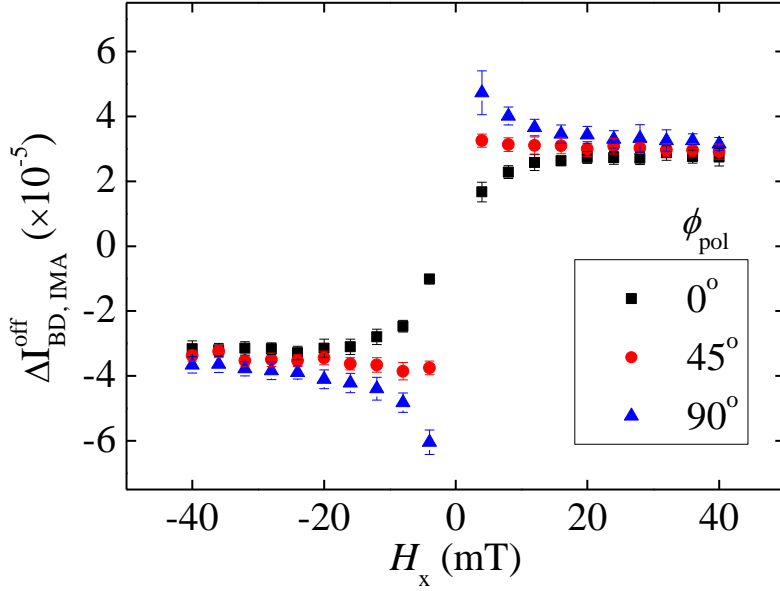


Figure 4.3.2 The SOT-induced signal $\Delta I_{BD, IMA}^{off}$ from different polarization angles ϕ_{pol} . The nearly constant feature of $\Delta I_{BD, IMA}^{off}$ at $\phi_{pol} = 45^\circ$ is from pMOKE whereas the $1/H_x$ feature at 0° and 90° is from optic PHE.

The coefficients of pMOKE and optic PHE for the Pt/Py bilayer sample have been calibrated through comparisons of the SOT components H_L (H_T) with the Oersted field (calibration field $H_{y, cal} = 4.5$ Oe) as performed in Ref. [46]. The longitudinal (transverse) components of the SOT are H_L (H_T) ~ 3 (2.4) Oe at current density of $3.1 \times 10^{10} A/m^2$. The obtained values of the coefficients are $\alpha_{pMOKE} = 3.3 \times 10^{-2}$ and $\beta_{PHE} = 1 \times 10^{-4}$. By measuring the intensity change from the rotation of the HWP2, the measured voltage from the optical signal has been normalized to the dimensionless quantity required for the calibration

process.

By contrast, when PEM is turned on, the incident light on the sample has a polarization state that oscillates between linear and circular polarization. Then, the harmonic signals with modulation frequency ω are measured using the LIA. The intensity measured by BD becomes

$$I_{BD}^{on} = -\beta_{PHE} \sin^2 \theta_M \sin(2(\phi_{pol} - \phi_M)) - 2\alpha_{pMOKE} \cos \theta_M \cos\left(\frac{\pi}{2} \cos(\omega t)\right). \quad (4.7)$$

Then, the Fourier expansion of Eq. (4.7) to the second order is written as

$$I_{BD,LIA}^{on} = A_{DC} + A_{2f} \cos(2\omega t), \quad (4.8)$$

where

$$A_{DC} = -\beta_{PHE} \sin^2 \theta_M \cos\left(2(\phi_{pol} - \phi_M)\right) - 2\text{BesselJ}\left[0, \frac{\pi}{2}\right] \alpha_{pMOKE} \cos \theta_M \quad \text{and} \quad A_{2f} = 4\text{BesselJ}\left[2, \frac{\pi}{2}\right] \alpha_{pMOKE} \cos \theta_M .$$

Here, BesselJ is a Bessel function of the first kind. It is surprising to note that the optic PHE signal is eliminated in A_{2f} of Eq. (4.8), and thus, only the pMOKE signal

remains. Finally, the SOT-induced signal with A_{2f} can be written as

$$\Delta A_{2f} = -4\text{BesselJ}\left[2, \frac{\pi}{2}\right] \alpha_{\text{pMOKE}} \sin\theta_M \Delta\theta_M \quad (4.9)$$

Note that A_{2f} measurement reduces the analysis complexity because only $\Delta\theta_M$ is involved in the measured SOT signal. This single-principle measurement is free from the PHE-related problems that occur in electrical SOT measurement methods.

Upon combining Eqs. (4.5) with (4.9), the magnitude of the SOT-induced signal in the IMA sample becomes

$$\Delta A_{2f, \text{IMA}} = -4\text{BesselJ}\left[2, \frac{\pi}{2}\right] \alpha_{\text{pMOKE}} \frac{H_L}{H_x - H_K^{\text{eff}}}. \quad (4.10)$$

To verify Eq. (4.10) experimentally, the amplitudes A_{2f} with $\pm J$ have been measured and subtracted. A laser beam spot has been located at the center of the wire to minimize the effect of the Oersted field $H_{Oe,z}$. The proportionality of the SOT induced signals for PEM on state to the current density J has been checked as shown in Figure 4.3.3.

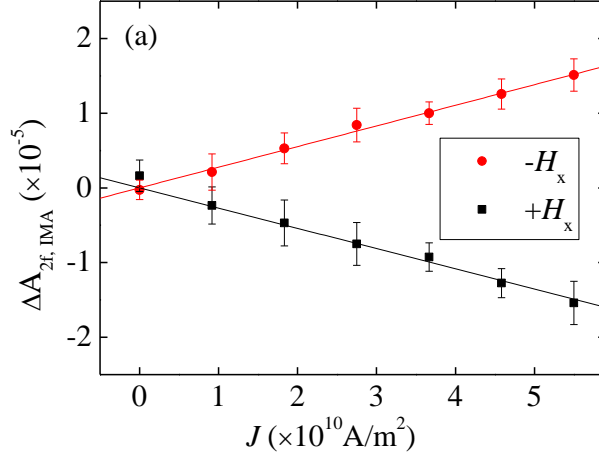


Figure 4.3.3 Linear proportionality of the SOT-induced signal $\Delta A_{2f, IMA}$ with respect to current density J at $H_x = 100$ mT. Red and black lines are linear fits to the data with zero intercept.

To confirm the separation between the pMOKE and optic PHE, the SOT induced signals with respect to ϕ_{pol} have been measured for two configurations of the PEM on/off states. For the case of $\Delta I_{BD, IMA}^{off}$ in Eq. (4.6), ϕ_{pol} dependency of the SOT induced signal consists of (1) sinusoidal dependence of optic PHE part and (2) constant of pMOKE part, whereas $\Delta A_{2f, IMA}$ in Eq. (4.10) with pure pMOKE signal has no dependency on ϕ_{pol} . Figure 4.3.4 confirms these two ϕ_{pol} dependencies of the SOT induced signals for the PEM on/off states. Elimination of the sinusoidal optic PHE signal shows qualitative and quantitative agreement

between (4.6) and (4.10) by considering the factor $2\text{BesselJ}\left[2, \frac{\pi}{2}\right] \sim 0.499$.

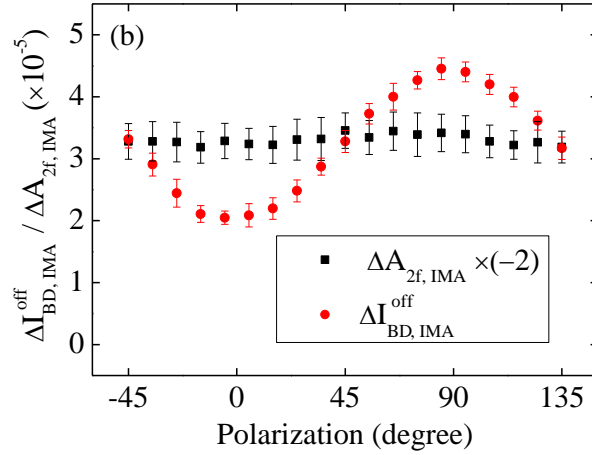


Figure 4.3.4 Comparison of the two SOT-induced signals $\Delta A_{2f, IMA}$ and $\Delta I_{BD, IMA}^{off}$ with respect to polarization angle ϕ_{pol} at $H_x = 8$ mT. $\Delta A_{2f, IMA}$ has no ϕ_{pol} dependence whereas $\Delta I_{BD, IMA}^{off}$ has sinusoidal dependence from optic PHE.

It is worthwhile to note that the selection of the beam splitter (BS) in the optic setup plays an important role in optic PHE signal elimination. If the reflectance (or transmittance) for s and p polarizations at the BS differs by a small value a , the optic PHE signal is included in the signal as given by

$$A_{2f,BS} = 4\text{BesselJ}\left[2, \frac{\pi}{2}\right] \left\{ \alpha_{\text{pMOKE}} \cos\theta_M + a\beta_{\text{PHE}} \sin^2\theta_M \cos 2(\phi_{\text{pol}} - \phi_M) \right\}. \quad (4.11)$$

To reduce this effect, the BS is selected with equal reflectance and transmittance for s and p polarizations. A cube-type BS is better in this respect owing to its relatively smaller a value in comparison to a plate-type BS. With the typical value of a ($=10^{-2} \sim 10^{-3}$), a cube-type BS generates negligible optic PHE effect in the experimental signal.

4.4 Discussion for Elimination of Optic PHE and Optic ANE

To explain the major origin of optic PHE elimination in the A_{2f} signal, a reduced setup has been introduced without HWPs. Further, the initial polarization, PEM major axis, and analyzer angles for BD are rotated by 45° for simplicity of calculation. Now, an initial horizontal polarization $\begin{pmatrix} 1 \\ 0 \end{pmatrix}$ passes through the PEM with major axis of 45° , and then, the light becomes $\vec{E}_i = \begin{pmatrix} \cos(\theta_{\text{PEM}}) \\ \sin(\theta_{\text{PEM}}) \end{pmatrix}$, where θ_{PEM} is the modulation amplitude of retardation at PEM. After reflection from the sample with

$$\vec{M}_{\text{sample}} = \begin{pmatrix} 1 + \frac{1}{2}B\cos(2\phi_M) & \theta_K + \frac{1}{2}B\sin(2\phi_M) \\ -\theta_K + \frac{1}{2}B\sin(2\phi_M) & 1 - \frac{1}{2}B\cos(2\phi_M) \end{pmatrix}, \quad (4.12)$$

where $B = \beta_{\text{PHE}} \sin^2 \theta_M$ from optic PHE and θ_K from pMOKE, the resultant electric field of light \vec{E}_r consists of four components as given by

$$\vec{E}_r = \begin{pmatrix} \cos(\theta_{\text{PEM}}) \\ \text{i} \sin(\theta_{\text{PEM}}) \end{pmatrix} + B \cos(2\phi_{\text{M}}) \begin{pmatrix} \cos(\theta_{\text{PEM}}) \\ -\text{i} \sin(\theta_{\text{PEM}}) \end{pmatrix} + B \sin(2\phi_{\text{M}}) \begin{pmatrix} \text{i} \sin(\theta_{\text{PEM}}) \\ \cos(\theta_{\text{PEM}}) \end{pmatrix} - \theta_{\text{K}} \begin{pmatrix} -\text{i} \sin(\theta_{\text{PEM}}) \\ \cos(\theta_{\text{PEM}}) \end{pmatrix}, \quad (4.13)$$

with (1) a normal reflection component without any polarization change, (2) a time reversal component from optic PHE with $\cos(2\phi_{\text{M}})$, (3) a spatial reversal component from optic PHE with $\sin(2\phi_{\text{M}})$, and (4) a spatial/time reversal component from pMOKE with θ_{K} . With BD with analyzer angle $\theta_{\text{A}} = \pm 45^\circ$, the measured intensity from each photodiode becomes

$$I_{\pm 45^\circ}^{\text{on}} = \frac{1}{2} \{1 + (\pm 2\theta_{\text{K}} + B \cos(2\phi_{\text{M}})) \cos(\theta_{\text{PEM}}) \mp B \sin(2\phi_{\text{M}})\}. \quad (4.14)$$

The time reversal part of Eq. (4.13) with $\cos(2\phi_{\text{M}})$ gives the same intensity to both photodiodes and therefore it cancels out. The spatial reversal part of Eq. (4.13) with $\sin(2\phi_{\text{M}})$ has no PEM modulation term that could be measured at the DC signal. As a result, the balanced signal reproduces Eq. (4.7) for the reduced geometry.

$$I_{\text{BD}}^{\text{on}} = I_{-45^\circ}^{\text{on}} - I_{+45^\circ}^{\text{on}} = -2\theta_K \cos(\theta_{\text{PEM}}) + B\sin(2\phi_M). \quad (4.15)$$

Therefore, by using polarization modulation with PEM and BD, the optic PHE and pMOKE signals are separated, leaving a pure pMOKE signal in the measured $2f$ amplitude.

In addition to the optic PHE, the ANE is the second artifact that hinders exact analysis in the electrical SOT measurement method. The ANE in the electrical measurement has a geometry of $V_{xy} \propto \nabla T \cdot m_x$, where ∇T represents the heat flow in the film normal direction (\hat{z}) generated by Joule heating. Similarly, the ANE-like signal for optical measurement would have the form $E_y^{\text{optic ANE}} \propto \nabla T \cdot m_x$. Similar to the ANE signal in the electrical measurement that appears in the second harmonic signal, $E_y^{\text{optic ANE}}$ also appears in the second harmonic signal. This ANE-like optical response shares common geometry and frequency response with the magnetization-induced second harmonic generation (MSHG) measurement scheme [59-60]. However, the magnitude of the optical signal in the MSHG configuration is so small that a photomultiplier tube (PMT) with a color filter is needed for optical signal detection. Therefore, the optic ANE contributions would be negligible and will not affect the signal in the detector with photodiodes.

Even if the optic ANE signal is measured, the signal would be almost constant with $\pm J$ applied to the sample. This is because SOT-induced reorientation of magnetization $\Delta\hat{m}$ is much smaller compared to the total magnetization \hat{m} and $\vec{E}^{\text{optic ANE}} \propto \nabla T \times \hat{m}$. As seen in Figure 4.3.3, signals with odd dependence on J only survive in the analysis process when excluding any possible optic ANE signal from the final result.

4.5 Conclusion

In conclusion, we demonstrate an optical SOT measurement method that is free from the optic PHE and optic ANE. Because the optic PHE and optic ANE signals are systematically forbidden in the method, the present optical setup provides an effective way to measure accurate and artifact-free SOT effects. Further, this setup offers an accessible method, especially for widely used conventional PEM setups, due to the similarity between the two setups.

Chapter 5

Characterization of the magnetic samples

Measurement of the basic characteristics of the magnetic sample provides solid foundations for the researches built upon it. Introduction of the new characterization method enables new type of analysis, which could be combined with the results from existing characterization methods. For the characterization of the magnetic samples, a setup with magneto-transport measurement have been installed and scanning transmission electron microscopy (STEM) have been introduced. The electric measurement based on anomalous Hall effect (AHE) have been utilized to measure Curie temperature T_c and effective perpendicular magnetic anisotropy field H_K^{eff} . The cross-section STEM images of the Pt/Co/Pt sample were obtained to check the crystallinity and characteristics of the interface between layers.

5.1 Introduction of the Curie Temperature T_c Measurement System

The Curie temperature T_c is the critical temperature where the spontaneous magnetization in ferromagnetic sample disappears above it. The magnitude of the current density in the ferromagnetic sample is limited by temperature rise from the Joule heating. Therefore measurement of the Curie temperature T_c characterizes the thermal stability of the sample and defines the range of the current applicable to the sample. Characterization of the thermal stability is crucial since T_c in ultrathin films have values that are close to the room temperature.

The measurement of T_c is realized by analysis of the hysteresis loops of the sample with increasing temperature [61]. An electric measurement system with cryostat, temperature controller (Cryocon), electromagnet, current source (Keithley 6221) and nano-voltmeter (Keithley 2182) has been established as shown in Figure 5.1.1.

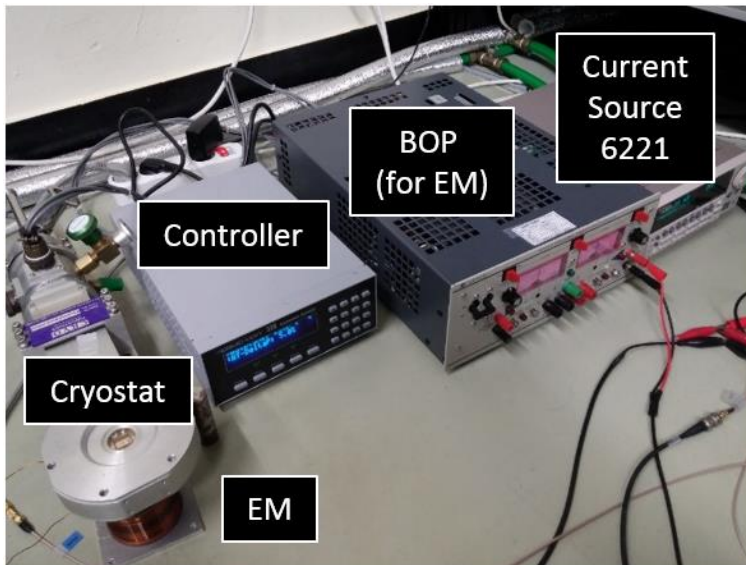


Figure 5.1.1 An electric measurement system for characterization of T_c . Hysteresis loop of the sample is measured with voltage from AHE.

The temperature control of the cryostat is done by balancing the heat flow from coolant (liquid helium or nitrogen) and PID-controlled electric heater. Within the upper limit of the cryostat temperature of 500K, hysteresis loops have been electrically measured to obtain the value of remanent magnetization m_r . The relative magnitude of m_r could be extracted by subtracting two values of R_{Hall} at zero H_z as shown in Figure 5.1.2.

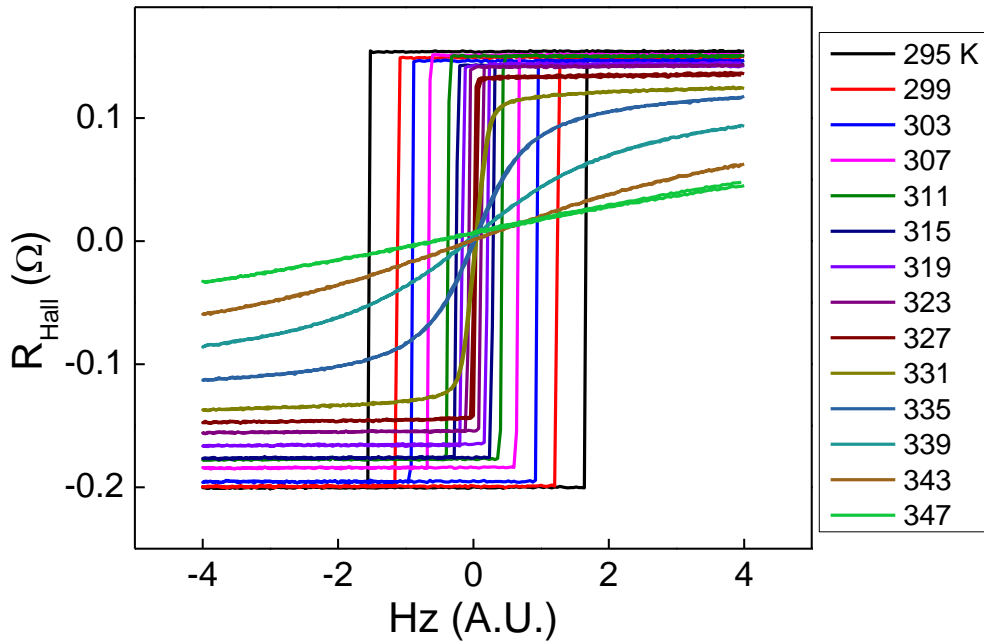


Figure 5.1.2 The hysteresis loops of the 5-nm Ta/2.5-nm Pt/0.3-nm Co/3.5-nm Pt sample with respect to the increasing temperature from 295 K to 347 K.

As temperature of the cryostat increases, the magnitude of the remanent magnetization decreases due to the thermal activation. The gradual decreasing value of $R_{\text{Hall}}(H_z = 0)$ with increasing cryostat temperature could be seen in Figure 5.1.2 and the values of the normalized remanent magnetization m_r with respect to temperature for $t_{\text{Co}} = 0.3, 0.35, 0.4, 0.45$ nm has been shown in Figure 5.1.3.

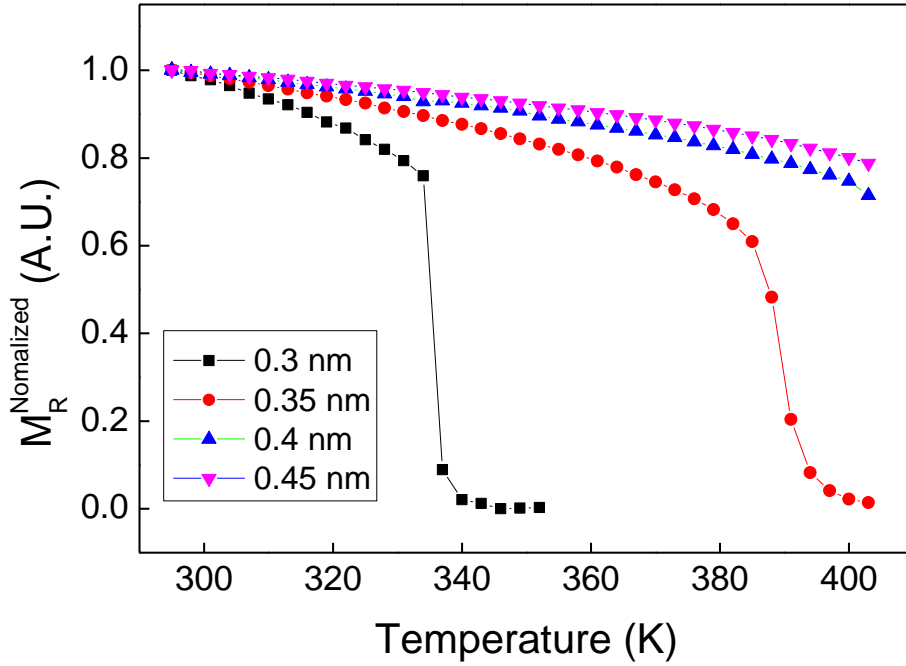


Figure 5.1.3 The plot of normalized remanent magnetization m_r with respect to temperature for 5-nm Ta/2.5-nm Pt/ t_{co} -nm Co/3.5-nm Pt samples with $t_{co}=0.3, 0.35, 0.4, 0.45$ nm.

As shown in Figure 5.1.3, abrupt decrease of m_r occurs around 340K for $t_{co}=0.3$ nm and around 390K for $t_{co}=0.35$ nm. The plot implies increasing Curie temperature T_c within increasing t_{co} . Exact value of T_c in this measurement could be obtained by fitting the data with formula of

$$m_r = \alpha \left(1 - \frac{T}{T_c}\right)^\beta, \quad (5.1)$$

with two fitting parameters α and β [61]. By the introduction of the T_c measurement method, thermal stability that sets the upper limit of the current density could be characterized.

5.2 Improvement on Perpendicular Anisotropy Field H_K Measurement Method

An effective perpendicular magnetic anisotropy (PMA) field H_K^{eff} is one of the important quantities analyzing the dynamics of magnetization for samples with perpendicular or in-plane magnetic anisotropy. Many methods have been proposed to quantify H_K^{eff} by electrical or optical measurement [62-63]. Stoner-Wohlfarth model that assumes uniaxial anisotropy and single domain state is used to describe the behavior of the magnetization. Under the external in-plane field of H_y , out-of-plane component of the magnetization m_z with PMA becomes

$$m_z = \sqrt{1 - \left(\frac{H_y}{H_K^{\text{eff}}}\right)^2}. \quad (5.2)$$

The magnitude of m_z can be obtained by measuring AHE signal in transverse voltage V_{xy} . Figure 5.2.1 represents decreasing of the m_z with increasing value of H_y due to the tilting of the magnetization. Fitting data with Eq. 5.2, value of the H_K^{eff} is obtained to be 7160 Oe that is in agreement with 7200 Oe, the result of method by ref. [62].

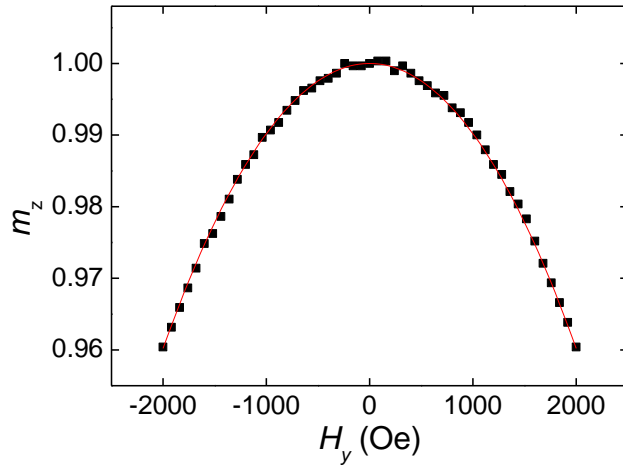


Figure 5.2.1 Out-of-plane magnetization m_z with respect to in-plane magnetic field H_y . The red solid line represents fitting of the data with Eq. 5.2.

5.3 TEM Image Measurement

A cross-sectional STEM image has been measured to obtain information about the crystalline structure and the upper/lower interface of the magnetic layer of the sample. A metallic stack with sample structure of 5-nm Ta/2.5-nm Pt/1.1-nm Co/1.5-nm Pt on top of Si/SiO₂ substrate has been fabricated with DC magnetron sputtering system. A microtome is prepared by focused ion beam (FIB) and NanoMill (Model 1040, Fishione Instruments). STEM image as well as a color map from energy-dispersive X-ray spectroscopy (EDS) analysis have been obtained as Figure 5.3.1.

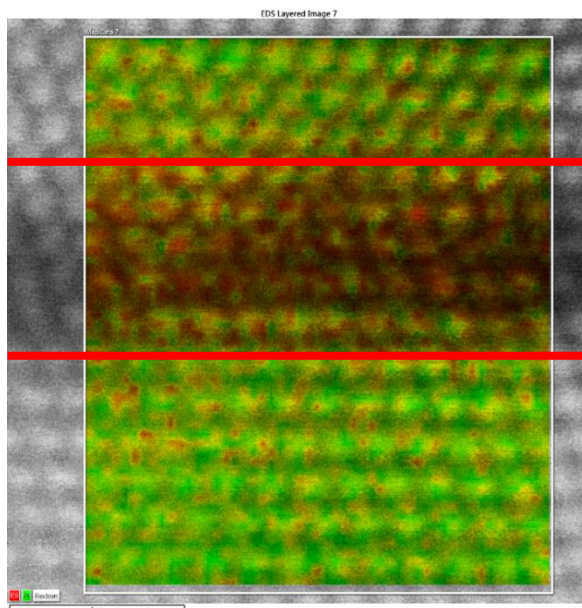


Figure 5.3.1 Cross-sectional STEM image with EDS color map of the Pt/Co/Pt sample. The red lines represent the upper and lower interface of the Co layer. Image was taken by Cs-STEM with operation of S.-P. Cho from NCIRF.

Appendix

A.1 Jones matrix calculation

Jones matrices for optical elements

To check the possibility of the elimination of the optic PHE signal, the measured intensity for various setups has been calculated using the Jones matrix formalism. The interaction of light with optical components could be represented by the Jones matrix product with the Jones vector of the initial polarization state. Table A.1.1 shows Jones matrices of optical components such as retarders, the sample, polarizers, and beam splitters.

	Retarders w/ phase retardation Γ	Sample	Polarizer	Beam splitter
Jones Matrices	$\vec{M}_{RT}(\Gamma)$ $= \begin{pmatrix} e^{-i\Gamma/2} & 0 \\ 0 & e^{i\Gamma/2} \end{pmatrix}$ $\Gamma_{HWP} = \pi,$ $\Gamma_{PEM} = \frac{\pi}{2} \cos\omega t$	\vec{M}_{sample} $= \begin{pmatrix} 1 + \frac{B}{2} & \theta_K \\ -\theta_K & 1 - \frac{B}{2} \end{pmatrix}$ $B = \beta_{PHE} \sin^2 \theta_M$	\vec{M}_P $= \begin{pmatrix} 1 & 0 \\ 0 & 0 \end{pmatrix}$	\vec{M}_{BS} $= \begin{pmatrix} 1 & 0 \\ 0 & 1 \end{pmatrix}$

Table A.1.1 Jones matrices of optical components. The Jones matrices of retarders and polarizers

are expressed as their major axis parallel to the x-axis of the Jones vector of $\begin{pmatrix} E_x \\ E_y \end{pmatrix}$. \vec{M}_{sample} is expressed with the direction of the in-plane magnetization parallel to the x-axis. When retarders, polarizers, and the sample are rotated, the rotated Jones matrix could be represented as $\vec{M}(\theta) = \vec{R}(\theta)\vec{M}\vec{R}(-\theta)$ with rotation matrix $\vec{R}(\theta) = \begin{pmatrix} \cos\theta & -\sin\theta \\ \sin\theta & \cos\theta \end{pmatrix}$.

Detailed intensity calculation using Jones calculus

The measured intensity with PEM turned off $I_{\text{BD}}^{\text{off}}$ can be calculated as follows.

With initial polarization of $\vec{E}_i = \frac{1}{\sqrt{2}} \begin{pmatrix} 1 \\ 1 \end{pmatrix}$, light goes through the optical path with PEM (no retardation), BS, HWP1, sample, HWP1, and BS to give final polarization \vec{E}_f as

$$\begin{aligned} \vec{E}_f &= \vec{M}_{\text{BS}}\vec{M}_{\text{RT}}(\pi, \phi_{\text{HW}})\vec{M}_{\text{sample}}(\phi_{\text{M}})\vec{M}_{\text{RT}}(\pi, \phi_{\text{HW}})\vec{M}_{\text{BS}}\vec{E}_i \\ &= \frac{1}{\sqrt{2}} \begin{pmatrix} -1 + \theta_{\text{K}} - \frac{B}{2}(\cos 2(2\phi_{\text{HW}} - \phi_{\text{M}}) + \sin 2(2\phi_{\text{HW}} - \phi_{\text{M}})) \\ -1 - \theta_{\text{K}} + \frac{B}{2}(\cos 2(2\phi_{\text{HW}} - \phi_{\text{M}}) - \sin 2(2\phi_{\text{HW}} - \phi_{\text{M}})) \end{pmatrix}, \end{aligned}$$

(A1)

where $\vec{M}_{\text{RT}}(\pi, \phi_{\text{HW}})$ represents $\vec{R}(\phi_{\text{HW}})\vec{M}_{\text{RT}}(\pi)\vec{R}(-\phi_{\text{HW}})$ and $\vec{M}_{\text{sample}}(\phi_{\text{M}})$ represents $\vec{R}(\phi_{\text{M}})\vec{M}_{\text{sample}}\vec{R}(-\phi_{\text{M}})$. The measured intensity from BD after the

analyzer within the first order of θ_K and B becomes

$$\begin{aligned}
I_{\text{BD}}^{\text{off}} &= |E_x|^2 - |E_y|^2 \\
&= -2\theta_K + B \cos 2(2\phi_{\text{HW}} - \phi_M) \\
&= -2\alpha_{\text{pMOKE}} \cos \theta_M - \beta_{\text{PHE}} \sin^2 \theta_M \sin 2(\phi_{\text{pol}} - \phi_M), \quad (\text{A2})
\end{aligned}$$

where $\phi_{\text{pol}} = 2\phi_{\text{HW}} - \frac{\pi}{4}$, $\theta_K = \alpha_{\text{pMOKE}} \cos \theta_M$, and $B = \beta_{\text{PHE}} \sin^2 \theta_M$.

Similarly, the measured intensity with PEM turned on $I_{\text{BD}}^{\text{on}}$ can be calculated as

$$\vec{E}'_f = \vec{M}_{\text{BS}} \vec{M}_{\text{RT}}(\pi, \phi_{\text{HW}}) \vec{M}_{\text{sample}}(\phi_M) \vec{M}_{\text{RT}}(\pi, \phi_{\text{HW}}) \vec{M}_{\text{BS}} \vec{M}_{\text{RT}}(\Gamma_{\text{PEM}}, 0) \vec{E}_i, \quad (\text{A3})$$

giving

$$I_{\text{BD}}^{\text{on}} = -\beta_{\text{PHE}} \sin^2 \theta_M \sin(2(\phi_{\text{pol}} - \phi_M)) -$$

$$2\alpha_{\text{pMOKE}}\cos\theta_{\text{M}}\cos\left(\frac{\pi}{2}\cos(\omega t)\right). \quad (\text{A4})$$

As shown in Eq. (4.11) in Chapter 4, the optic PHE contribution is measured in the PEM on state when the reflectance (or transmittance) for s and p polarization have different values. The measured intensity could be calculated by the modified Jones matrix of BS. The difference a of the reflectance (or transmittance) for s and p polarization could be represented by $\vec{M}_{\text{BS}}(a) =$

$$\begin{pmatrix} 1 + \frac{a}{2} & 0 \\ 0 & 1 - \frac{a}{2} \end{pmatrix} \text{ to give}$$

$$A_{2f,\text{BS}} = 4\text{BesselJ}\left[2, \frac{\pi}{2}\right] \left\{ \alpha_{\text{pMOKE}}\cos\theta_{\text{M}} + a\beta_{\text{PHE}}\sin^2\theta_{\text{M}}\cos 2(\phi_{\text{pol}} - \phi_{\text{M}}) \right\}. \quad (\text{A5})$$

Note that the sign of a upon transmission in $\vec{M}_{\text{BS}}(a)$ should be different from the sign of a upon reflection because the sum of transmittance and reflectance should be unity.

References

- [1] S. S. P. Parkin et al., *Science* 320, 190-194 (2008).
- [2] M. Hayashi et al., *Science* 320, 209 (2008).
- [3] L. Thomas et al., *Science* 330, 1810 (2010).
- [4] K.-J. Kim et al., *Appl. Phys. Express* 3, 083001 (2010).
- [5] D. A. Allwood et al., *Science* 309, 1688 (2005).
- [6] A. Fert et al., *Nat. Nanotech.* 8, 152 (2013).
- [7] P. P. J. Haazen et al., *Nat. Mater.* 12, 299-303 (2013).
- [8] S.-G. Je et al., *Phys. Rev. B* 88, 214401 (2013).
- [9] S.-W. Jung et al., *Appl. Phys. Lett.* 92, 202508 (2008).
- [10] A. A. Thiele et al., *Phys. Rev. Lett.* 30, 230 (1973)
- [11] E. Saitoh et al., *Nature* 432, 203 (2004)
- [12] A. Thiaville et al., *Europhys. Lett.* 100, 57002 (2012).
- [13] A. V. Khvalkovskiy et al., *Phys. Rev. B* 87, 020402(R) (2013).
- [14] S. Emori et al., *Nat. Mater.* 12, 611-616 (2013).
- [15] K.-S. Ryu et al., *Nat. Nanotech.* 8, 527-533 (2013).
- [16] S.-M. Seo et al., *Appl. Phys. Lett.* 101, 022405 (2012).
- [17] J. C. Lee et al., *Phys. Rev. Lett.* 107, 067201 (2011).
- [18] U. H. Pi et al., *Appl. Phys. Lett.* 97, 162507 (2010).
- [19] J. Kim et al., *Nat. Mater.* 12, 240 (2013).
- [20] K. Garello et al., *Nat. Nanotech.* 8, 587 (2013).
- [21] X. Fan et al., *Nat. Commun.* 4, 1799 (2013).
- [22] X. Fan et al., *Nat. Commun.* 5, 3042 (2014).
- [23] S. J. Yun et al., *J. Magn.* 25, 1 (2015).

- [24] M. Hayashi et al., Phys. Rev. B 89, 144425 (2014).
- [25] Y. Fan et al., Nat. Mater. 13, 699 (2014).
- [26] M. Montazeri et al., Nat. Commun. 6, 8958 (2015).
- [27] T. Schulz et al., Phys. Rev. B 95, 224409 (2017).
- [28] J. Kerr, Philos. Mag. 3, 321 (1877).
- [29] Mansuripur, The Physical Principles of Magneto-optical Recording, Chapter 5
- [30] C.-Y. You and S.-C. Shin, Appl. Phys. Lett. 69 (9) (1996)
- [31] 16. E. Hall, Philos. Mag. 12, 157 (1879).
- [32] T. R. McGuire and R. I. Potter, IEEE Trans. Magn. 11, 1018 (1975).
- [33] S. Cho et al., Sci. Rep. 5, 14668 (2015)
- [34] L. Berger, J. Appl. Phys. 55, 1954 (1984).
- [35] J. Slonczewski, J. Magn. Magn. Mater. 159, L1 (1996).
- [36] A. Yamaguchi et al., Phys. Rev. Lett. 92, 077205 (2004).
- [37] I. M. Miron et al., Nat. Mater. 10, 419 (2011).
- [38] M. Jamali et al., Phys. Rev. Lett. 111, 246602 (2013).
- [39] T. Suzuki et al., Appl. Phys. Lett. 98, 142505 (2011).
- [40] K.-W. Kim et al., Phys. Rev. B 85, 180404(R) (2012).
- [41] I. M. Miron et al., Nature 476, 189 (2011).
- [42] L. Liu et al., Science 336, 555 (2012).
- [43] L. Liu et al., Phys. Rev. Lett. 109, 096602 (2012).
- [44] C.-F. Pai et al., Phys. Rev. B 93, 144409 (2016)

- [45] T.-Y. Chen et al., Phys. Rev. Appl. 10, 044038 (2018)
- [46] X. Fan et al., Appl. Phys. Lett. 109, 122406 (2016).
- [47] J. H. Franken et al., Sci. Rep. 4, 5248 (2014).
- [48] S. Emori et al., Phys. Rev. B 90, 184427 (2014).
- [49] S.-G. Je et al., Phys. Rev. Lett. 118, 167205 (2017).
- [50] S.J. Yun et al., NPG Asia Mater. 9, e449 (2017).
- [51] C. O. Avci et al., Phys. Rev. B 90, 224427 (2014).
- [52] B. F. Miao et al., Phys. Rev. Lett. 112, 236601 (2014).
- [53] W. X. Wang et al., Appl. Phys. Lett. 105, 182403 (2014).
- [54] K. Sato, Jpn. J. Appl. Phys. 20, 2403 (1981).
- [55] K. Postava et al., J. Eur. Opt. Soc.-Rapid 1, 06017 (2006).
- [56] A. J. Schellekens et al., Phys. Rev. B 90, 104429 (2014).
- [57] C. A. Nwokoye et al., J. Magn. Magn. Mater. 421, 230-233 (2017).
- [58] Y. Yang et al., Sci. Adv. 3:e1603117 (2017).
- [59] S. Vandendriessche et al., Appl. Opt. 51, 209-213 (2012).
- [60] I. A. Kolmychek et al., J. Magn. Magn. Mater. 323, 2973 (2011).
- [61] T. Koyama et al., Appl. Phys. Lett. 106, 132409 (2015).
- [62] K. W. Moon et al., Rev. Sci. Instrum. 80, 113904 (2009).
- [63] H. S. Whang et al., J. Magn. 20, 8 (2015).

국문 초록

스핀-궤도 돌림힘이란 스핀-궤도 상호작용을 가지는 물질에서 발생한 스핀 전류가 자화에 영향을 주는 현상을 말한다. 스핀-궤도 돌림힘을 이용하면 자기장이 아닌 전류를 사용해 자화의 제어가 가능하기 때문에, 자화 기반 메모리의 소형화에 필수적인 요소로 많은 관련 연구가 진행되어 왔다. 스핀-궤도 돌림힘은 자화역전, 전류구동 자구벽 운동, 스핀돌림힘 강자화공진, 교류 전류에 의한 자화 진동 등의 현상을 통해 측정될 수 있다. 서로 다른 물리적 상황을 가지는 여러 가지 측정에서 얻은 스핀-궤도 돌림힘에 대한 다양한 측정값이 제시되었다.

여러 결과를 비교하여 정확한 스핀-궤도 돌림힘 측정값을 얻을 수 있도록 스핀-궤도 돌림힘 측정법 간의 결과를 교차 검증할 수 있도록 하는 연구를 수행하였다. 2종의 자구벽 운동 기반 측정법과 자화진동 기반 측정법, 총 3가지 측정법을 통해 측정값을 얻었고, 7가지 물질을 사용한 시료군에서의 결과를 교차 검증하여 이론적으로 예측되었던 변환 인자를 실험적으로 증명하였다.

또한 기존의 스핀-궤도 돌림힘 측정법에서 분석에 어려움을 주던 문제를 해결하기 위해 부수효과가 제거된 새로운 광학적 측정법을 개발

하였다. 널리 쓰이는 전기적 측정법에서 나타나는 부수효과인 평면 홀 효과와 특이한 네른스트 효과가 광학적 대칭성을 이용해 제거된 실험 장치를 고안하였다. 이 측정법은 측정신호를 얻고 후처리 방법으로만 제거되던 부수효과를 측정 단계부터 제외시킬 수 있는 장점이 있다.

측정법간의 상호 검증과 부수효과가 제거된 새로운 측정법을 개발은 더 넓은 조건에서 다양한 시료에 대한 스핀-궤도 돌림힘 연구를 가능하게 하여 학문적, 응용적 연구에 도움이 될 것이라 기대한다.

주요어 : 스핀-궤도 돌림힘, 광자기 커르 효과, 평면 홀 효과, 특이한 네른스트 효과,
전류 구동 자구벽 운동

학번 : 2013-20363

Publications

1. Cheong-Gu Cho, Joon Moon, **Joo-Sung Kim** and Sug-Bong Choe, Cheol-Hyun Moon and Byoung-Chul Min, Sang-Il Kim and Seung-Young Park, “Optimization of the Gilbert damping constant by annealing CoFeB films sandwiched by Ta, Ru, and Pd layers”, J. Kor. Phys. Soc. **65(10)**, 1161-1613 (2014).
2. Soong-Geun Je, Sang-Cheol Yoo, **Joo-Sung Kim**, Yong-Keun Park, Min-Ho Park, Joon Moon, Byoung-Chul Min, and Sug-Bong Choe, “Emergence of Huge Negative Spin-Transfer Torque in Atomically Thin Co Layers”, Phys. Rev. Lett. **118**, 167205 (2017)
3. **Joo-Sung Kim**, Yune-Seok Nam, Dae-Yun Kim, Yong-Keun Park, Min-Ho Park, and Sug-Bong Choe, “Comparison between spin-orbit torques measured by domain-wall motions and harmonic measurements”, AIP Adv. **8**, 056009 (2018)
4. Dae-Yun Kim, Min-Ho Park, Yong-Keun Park, **Joo-Sung Kim**, Yune-Seok Nam, Hyeok-Cheol Choi, Duck-Ho Kim, Soong-Geun Je, Byoung-Chul Min, and Sug-Bong Choe, “Chirality-induced antisymmetry in domain-wall speed”, NPG Asia Mater. **10**, e464 (2018)
5. Dae-Yun Kim, Min-Ho Park, Yong-Keun Park, Ji-Sung Yu, **Joo-Sung Kim**, Duck-Ho Kim, Byoung-Chul Min, and Sug-Bong Choe, “Huge domain-wall speed variation with respect to ferromagnetic layer thickness in Ferromagnetic Pt/Co/TiO₂/Pt films”, Appl. Phys. Lett. **112**, 062406 (2018)
6. Dae-Yun Kim, Min-Ho Park, Yong-Keun Park, **Joo-Sung Kim**, Yune-Seok Nam, Hyun-Seok Whang, Hyeok-Cheol Choi, Duck-Ho Kim, Soong-Geun Je, Byoung-Chul Min, and Sug-Bong Choe, “Magnetic domain-wall tilting due to domain-wall speed asymmetry”, Phys. Rev. B **97**, 134407 (2018),
7. Yong-Keun Park, Dae-Yun Kim, **Joo-Sung Kim**, Yune-Seok Nam, Min-Ho Park, Hyeok-Cheol Choi, Byoung-Chul Min, and Sug-Bong Choe, “Experimental observation of the correlation between interfacial Dzyaloshinskii-Moriya interaction and work function in metallic magnetic trilayers”, NPG Asia Mater. **10**, 995-1001 (2018)
8. **Joo-Sung Kim**, Yong-Keun Park, Hyun-Seok Whang, Jung-Hyun Park, Byoung-Chul Min, and Sug-Bong Choe “Artifact-free optical spin-orbit torque magnetometry”, in preparation

Conferences

Korean

1. 20140423, 2014 한국 물리학회 봄 학술논문발표회, Dajeon, Korea, P1-D002, Joo-Sung Kim, Soong-Geun Je, Sang-Cheol Yoo, Byoung-Chul Min, and Sug-Bong Choe, “스핀-궤도 토크를 이용한 Pt/Co/Pt 박막의 자구벽 운동 속도 향상”
2. 20150528, 2015 한국 자기학회 하계학술대회, Busan, Korea, O-I-5, Joo-Sung Kim, Soong-Geun Je, Sang-Cheol Yoo, Joon Moon, Byoung-Chul Min, and Sug-Bong Choe, “Domain Wall Motion Driven by Negative Spin-Transfer Torque”
3. 20170419, 2017 한국 물리학회 봄 학술논문발표회, Joo-Sung Kim, Yune-Seok Nam, Dae-Yun Park, Min-Ho Park, Yong-Keun Park, and Sug-Bong Choe, “Different characteristics of spin-orbit torque between domain-wall motion and harmonic measurements”

International

1. 20151019, German-Korean Workshop, Seoul, Korea, Joo-Sung Kim, Joon Moon, Sang-Joon Yun, and Sug-Bong Choe, “Optical Measurement of Spin-Orbit Torque by use of Circularly Polarized Light”
2. 20151118, 13th RIEC International Workshop on Spintronics, Sendai-Japan, P-17, Joo-Sung Kim, Joon Moon, Sang-Joon Yun, and Sug-Bong Choe, “Optical Measurement of Spin-Orbit Torque by use of Circularly Polarized Light”
3. 20151128, Korea-Japan Spin-Orbit Workshop, Daejeon, Korea, P-18, Joo-Sung Kim, Joon Moon, Sang-Joon Yun, and Sug-Bong Choe, “Optical Measurement of Spin-Orbit Torque by use of Circularly Polarized Light”
4. 20161102, 61st Annual Conference on Magnetism and Magnetic Materials, New Orleans, USA, DV-05, Joo-Sung Kim, Seung-Heon Chris Baek, Byong-Guk Park, and Sug-Bong Choe, “Optical technique for spin-orbit torque measurement based on linear and circular polarizations”
5. 20161216, International School on Spintronics and Spin-Orbitronics, Fukuoka, Japan, Joo-Sung Kim, Seung-Heon Chris Baek, Byong-Guk Park, and Sug-Bong Choe, “Optical technique for spin-orbit torque measurement based on linear and circular polarizations”
6. 20171106, 62nd Annual Conference on Magnetism and Magnetic Materials, Pittsburgh,

USA, FS-07, Joo-Sung Kim, Yune-Seok Nam, Dae-Yun Park, Min-Ho Park, Yong-Keun Park, and Sug-Bong Choe, “Experimental Equivalence of Spin-Orbit Torque between Domain-Wall Motion and Harmonic Measurements”

7. 20180605, 5th International Conference of Asian Union of Magnetism Societies, Jeju, Korea, G1-0685, Joo-Sung Kim, Yune-Seok Nam, Dae-Yun Park, Min-Ho Park, Yong-Keun Park, and Sug-Bong Choe, “Experimental Equivalence of Spin-Orbit Torque between Domain-Wall Motion and Harmonic Measurements”